

Author Manuscript

This is the author manuscript accepted for publication and has undergone full peer review but has not been through the copyediting, typesetting, pagination and proofreading process, which may lead to differences between this version and the [Version of Record](#). Please cite this article as [doi: 10.1002/MP.13414](https://doi.org/10.1002/MP.13414)

This article is protected by copyright. All rights reserved

Cherenkov emission-based external radiotherapy dosimetry:

I. Formalism and feasibility

Yana Zlateva

*Medical Physics Unit, McGill University, Montreal, QC, H4A 3J1, Canada,**

Bryan R. Muir

Metrology Research Centre, National Research Council, Ottawa, ON, K1A 0R6, Canada,

Issam El Naqa

Department of Radiation Oncology, University of Michigan, Ann Arbor, MI, 48103-4943, USA, and

Jan P. Seuntjens

Medical Physics Unit, McGill University, Montreal, QC, H4A 3J1, Canada

(Dated: January 28, 2019)

Purpose: Cherenkov emission (CE)-based external beam dosimetry is envisioned to involve the detection of CE directly in water with placement of a high-resolution detector out of the field, avoiding perturbations encountered with traditional dosimeters. In this work, we lay out the groundwork for its implementation in the clinic and motivate CE-based dosimeter design efforts. To that end, we examine a formalism for broad-beam in-water CE-based dosimetry of external radiotherapy beams, design and test a Monte Carlo simulation framework for the calculation of CE-to-dose conversion factors used by the formalism, and demonstrate the experimental feasibility of this method.

Methods: The formalism is conceptually analogous to ionization-based dosimetry and employs CE-to-dose conversion factors, $k_C^{\theta \pm \delta\theta}$, including only and all CE generated within polar angles $\theta \pm \delta\theta$ on beam axis. The EGSnrc user code SPRRZnrc is modified to calculate $k_C^{\theta \pm \delta\theta}$, as well as CE spectral and angular distributions. The modified code is tested with monoenergetic parallel electrons on a thin water slab. Detector configurations are examined for broad 6-22 MeV electron beams from a BEAMnrc TrueBeam model, with a focus on $\theta \pm \delta\theta = 90^\circ \pm 90^\circ$ (4π detection), $90^\circ \pm 5^\circ$, and $42^\circ \pm 5^\circ$ ($\theta = 42^\circ$ is the CE angle of relativistic electrons in water). We perform a relative experimental validation at 90° with electron beams, using a simple detector design with spherical optics and geometrical optics approximation of the sensitive volume, which spans the water tank. Due to transient charged particle equilibrium, broad photon beams are generally less sensitive to beam quality, depth, and angle.

Results: For 0.1-50 MeV electrons on a thin water slab, the code outputs CE photon spectral density per unit mass (calculated from dose and $k_C^{\theta \pm \delta\theta}$) and angle in agreement with theory within $\pm 0.03\%$ and $\pm 0.01^\circ$, respectively, corresponding to the output precision. The 42° configuration was found impractical due to detection considerations. Detection at $90^\circ \pm \delta\theta$ for small $\delta\theta$ exhibited beam quality dependence of the same order as well as strong superficial depth dependence. A 4π configuration ameliorates these effects. A more practical approach may employ a large numerical aperture. In comparing with literature, we find that these effects are less pronounced for broad photon beams in water, as expected. Measured relative $k_C^{90^\circ \pm \delta\theta}$ at small $\delta\theta$ were within 1% of simulated factors (relative to their local average) for percent-depth CE (PDC) $> 50\%$. At other depths, deviations were in accordance with signal-to-noise, known detector limitations, and approximations. It was found that the CE spectrum is beam quality and depth invariant, while for electron beams the CE

angular distribution is strongly dependent on beam quality and depth. However, the uncertainty of CE and PDC measurement at $90^\circ \pm \delta\theta$ detection for small $\delta\theta$ due to $\pm 0.1^\circ$ deviations around $\delta\theta$ was shown to be $\leq 1\%$ and $< 0.1\%$ ($k = 1$), respectively. The robustness to expected detector setup variations was found to result in $\leq 1\%$ ($k = 1$) local uncertainty contribution for PDC $> 50\%$.

Conclusions: Based on our Monte Carlo and experimental studies, we conclude that the CE-based method is promising for high-resolution perturbation-free 3D dosimetry in water, with specific applications contingent on comprehensive detector development and characterization.

Author Manuscript

* yana.zlateva@mail.mcgill.ca; <http://www.mcgill.ca/medphys/>

I. INTRODUCTION

Current routine radiotherapy dosimetry methods employ non-water equivalent detectors, resulting in a necessary
 50 dose-to-water conversion as well as possibly significant field perturbation and volume averaging across the detection
 medium. In this work, we examine the feasibility of Cherenkov emission (CE)[1–3] dosimetry based on in-water CE
 detection with an out-of-field detector system with potential resolution of the order of micrometers.[4, 5] Despite
 recent progress,[6, 7] a clinically-implementable CE-based dosimetry system and protocol have not been established
 and data for converting CE to dose is not yet available. We motivate CE-based dosimetry detector and protocol
 55 development studies by considering a potential broad-beam[8] central-axis in-water CE-to-dose conversion formalism
 and modifying and experimentally evaluating EGSnrc[9] for the calculation of the broad-beam CE-to-dose conversion
 on beam axis in water, which is a useful starting point.

Quantitative studies of CE by external radiotherapy beams for the purpose of dosimetry have been published by
 Helo et al.[6] and Glaser et al.[7] Helo et al. investigate CE for use in quality assurance tests, such as range and
 60 field size verification of electron beams via Monte Carlo and experiment. They find that CE imaging can be used to
 predict the practical range to within 3 mm for the 6, 9, and 12 MeV clinical electron beams studied and to measure
 the field width at 50% of the maximum dose. They conclude that CE can be used for quick routine quality assurance
 spot checks of electron beam range and field width constancy. Glaser et al.[7] carry out Monte Carlo studies of CE by
 photon, electron, and proton beams in water. They state that in order for a CE-based dosimetry method to be viable,
 65 the CE-to-dose ratio must ideally be independent of position in the irradiated medium. They conclude that CE-based
 dosimetry is not feasible for clinical beams, with some exceptions including treatment plan verification of specialized
 applications such as VMAT and IMRT. Here, we confirm that CE-to-dose ratios are position-dependent and can be
 calculated via Monte Carlo for clinical beams. The primary objective of this work is to incorporate and examine,
 from first principles, the broad-beam CE-to-dose conversion in a mathematical context as part of a formalism.

Our work is organized into two complementary papers. In this paper (Paper I), we (1) present a potential broad-
 beam central-axis CE-to-dose conversion formalism, (2) design and test the Monte Carlo method for calculating
 conversion factors, and (3) validate our code through a relative experimental study with electron beams in water
 and with a simple detector design. The formalism applies to both photon and electron beams, while the calculation
 framework is validated experimentally with electron beams in water, for which we find that the relative conversion is
 75 more strongly dependent on depth, beam quality, and angle by comparison with the literature on broad photon beam
 CE-based dosimetry in water.[7, 10, 11] In the companion paper (Paper II),[12] which is motivated by the results
 of this paper (Paper I) and is focused entirely on electron beams, we calculate and examine the conversion for a
 clinically-representative library of validated electron beam models, address electron beam quality specification, and
 evaluate a potential dosimetric uncertainty budget at a reference depth in water.

II. SETUP AND FORMALISM

The setup we envision for CE-based dosimetry on beam axis in water is shown in Figure 1. The broad-beam CE-
 based formalism presented below applies to CE detection with narrow response on the beam axis, indicated by the
 square in Figure 1. This requires optical design and characterization of a dedicated CE detection system, potentially

including a customized phantom geometry and extension to 2D or 3D via focal spot scanning or a detector array. Out-of-focus removal and narrowing of the response at a distance from the optics is done in confocal microscopy as well as in optical section microscopy (without an excitation laser) by means of, e.g., nearest-neighbour de-blurring.[5] Detector development is beyond the scope of this work and will require a considerable amount of resources and further investigation. The aim of this paper is to motivate this investigation by examining the broad-beam CE-to-dose conversion on beam axis in water, from first principles and with a simple detector.

The clinical endpoint, e.g., CE-based absolute versus relative dosimetry, large versus small field dosimetry, and MR-linac applications, is a related issue as it requires detector design and characterization. Absolute conversion of CE to dose may be feasible in a controlled phantom environment. No matter the outcome of a detector development study, it is nevertheless of scientific interest to examine the absolute beam-axis CE-to-dose conversion for a broad-beam geometry in water.

To this end, we calculate the conversion via Monte Carlo and we validate our code through a relative experimental study with a simple detector, built in-house with two plano-convex lenses + apertures feeding into a multimode optical fiber, as outlined below in Section III B. Therefore, the sensitive volume spans the entire water tank, as indicated by the gray double cone in the water in Figure 1, and we compare Monte Carlo-calculated to measured CE depth scans within this large sensitive volume, approximated via ray optics and assuming uniform response across it.

We now describe a potential broad-beam central-axis CE-based dosimetry formalism. A sample schematic for this purpose is shown in Figure 2. Under reference conditions for which the calibration and conversion apply, we have a broad beam[8] of quality Q depositing dose D in a small volume on beam axis and generating an anisotropic CE signal.[3] A portion of the CE angular distribution within the polar angle range $\theta \pm \delta\theta$, defined by the optics angular aperture (discussed below), is sampled and detected as a reading M . The equation we propose for relating M to D under reference conditions is the following:

$$D(Q) = M N k_C^{\theta \pm \delta\theta}(Q), \quad (1)$$

where

$$M = M_{\text{raw}}(SSD, x, y, z, FS) P_T, \quad (1a)$$

$$k_C^{\theta \pm \delta\theta} = \frac{\int_{\Delta}^{E_{\text{max}}} \Phi_E(E) L_{\Delta}(E) dE + \Phi_E(\Delta) S_{\text{col}}(\Delta) \Delta}{\int_{E_{\text{thr}}}^{E_{\text{max}}} \Phi_E^{\theta \pm \delta\theta}(E) S_{\text{CE}}(E, \epsilon) dE}, \quad (1b)$$

$$S_{\text{CE}}(E, \epsilon) = \frac{\alpha}{\hbar c} \left(1 - \frac{1}{n(\epsilon)^2 \beta(E)^2} \right), \quad (1c)$$

where the involved quantities are defined as:

Q : beam quality specifier, which may or may not be the same as in current protocols[8, 13] based on the associated uncertainty contributions.

M : measured background-subtracted optical spectral density reading, M_{raw} , under the reference conditions of SSD , point of measurement, field size, FS , and temperature, T , for which the calibration and conversion apply. The temperature correction factor, P_T , stems from the temperature dependence of the refractive index, n , [14] and is discussed in greater detail in Paper II.[12]

- N : response calibration of the optical detector system, corresponding to the ratio of CE per unit mass generated at polar angles in the range $\theta \pm \delta\theta$ relative to the beam direction to detector reading. The angles are discussed below. The calibration would be obtained via a calibration lamp, traceable to a primary standards laboratory, and independent of ionizing radiation beam quality for optical systems with uniform response in the CE signal range, which may give CE-based dosimetry a distinct advantage over current methods.
- $k_C^{\theta \pm \delta\theta}$: CE-to-dose conversion factor, including only and all CE at polar angles in the range $\theta \pm \delta\theta$ relative to the beam direction, which is determined by the detection optics angular aperture (AA), i.e., the acceptance half-angle. The AA is defined as the angular size, relative to the optical axis, of the optical aperture as seen from the focal point. Because CE is anisotropic[3] and optics have a limited AA, it is necessary to consider the portion of the CE angular distribution sampled by the optics. Only polar angles are considered, because the azimuthal component of the optics AA can be made 2π via azimuthal integration (e.g., rotation about the beam axis) or it can be included in the calibration, N , (together with the detector response) and would not vary in the azimuthal direction for symmetric beams. This also serves to improve the simulation statistics.
- Δ : Spencer-Attix cut-off energy.[15]
- E_{thr} : CE threshold energy (260 keV over the visible spectrum in water).[3, 14]
- E_{max} : maximum particle kinetic energy at the point of measurement.
- Φ_E : total (primary and secondary) charged particle fluence spectrum, differential in energy, at the point of measurement.
- $\Phi_E^{\theta \pm \delta\theta}$: total fluence spectrum, differential in energy, of charged particles with CE polar angles in the range $\theta \pm \delta\theta$ at the point of measurement.
- L_Δ : charged particle restricted collision stopping power.
- S_{CE} : CE power, expressed as the Frank-Tamm differential[2] and defined as the CE photon count differential in CE energy, ϵ , and path length of a charged particle of energy E corresponding to velocity β (in units of the speed of light in vacuum, c).

Integration over charged particle types is implicit in Equation 1b. Note that in contrast to ion chamber dosimetry, where the measurement medium is a gas,[8, 16] pressure and humidity do not have any effect on M in CE-based dosimetry (see Equation 1a).

Equation 1 applies to both photon and electron beams. The conversion from M to CE at $\theta \pm \delta\theta$, including the system response and azimuthal AA, is contained in the system calibration N . The conversion from CE at $\theta \pm \delta\theta$ to D is contained in the CE-to-dose conversion factor $k_C^{\theta \pm \delta\theta}$. The $k_C^{\theta \pm \delta\theta}$ factor in Equation 1b is the ratio of dose according to Spencer-Attix theory[15] to CE per unit mass within $\theta \pm \delta\theta$, under reference conditions. Note that these should be mass stopping and CE powers, but the density of the cavity material is the same. In addition, the CE integral has no track-end term as there is no CE below the threshold E_{thr} .

The unrestricted collision stopping power[17] and CE power[2] (Equation 1c) are plotted as a function of electron kinetic energy in Figure 3 for energies in the range 0.1-10 MeV in water (Equation 1c with $n = 1.34$).[14] It is clear from this figure and from Equation 1b that the $k_C^{\theta \pm \delta\theta}$ factor is beam quality and depth dependent, because the stopping power and CE power are different functions of charged particle energy integrated from different low-energy thresholds in the charged particle fluence spectrum.

III. MATERIALS AND METHODS

A. Monte Carlo calculation of conversion factors

1. BEAMnrc model and parameters

Beams are simulated with the BEAMnrc code[18, 19] of the particle transport simulation package EGSnrc.[9, 20] The experimental validation study focuses on electron beams, which tests the limits of the code performance due to higher overall sensitivity to beam quality, depth, and angle than for photon beams.[7, 10, 11] Our clinical machine is a Varian TrueBeam, whose BEAMnrc model data and parameters were provided by the vendor (Virtual Linac, Varian Medical Systems, Inc., Palo Alto, CA).[21] Eight electron beams were simulated with nominal energies of 6-20 MeV and 22 MeV at $10 \times 10\text{-cm}^2$ and $20 \times 20\text{-cm}^2$ field size, respectively, and 100-cm SSD.[8]

2. SPRRZnrc modifications and parameters

BEAMnrc-generated incident phase space data were input into a modified version[22] of the SPRRZnrc code,[23] which calculates Spencer-Attix mass restricted collision stopping-power ratios[15] by summing contributions from charged particle steps on-the-fly. SPRRZnrc was adapted to calculate $k_C^{\theta \pm \delta\theta}$ factors according to Equation 1b by: (1) using a homogeneous water phantom; (2) modifying the code to score CE power within $\theta \pm \delta\theta$ in water instead of stopping power in a different medium;[2] and (3) setting the Spencer-Attix cut-off Δ for scoring the dose to 10 keV (electron CSDA range = $3 \mu\text{m}$ in water)[17] and the CE threshold for scoring CE to 257 keV for refractive index of 1.34,[2] which corresponds to a minimum (at 500 nm) in optical absorption by water at room temperature.[14, 24]

Detection of CE depends on the overlap of the detection geometry with the CE cone, which varies with charged particle energy and direction. A sample geometry for scoring CE by an electron with momentum unit vector $\hat{\mathbf{p}}_e = [\mathbf{u}, \mathbf{v}, \mathbf{w}]$, corresponding to CE cone angle $\cos \theta_{\text{CE}} = (n\beta)^{-1}$,[3] is shown in Figure 4. The CE photons generated within the polar angle range $\theta \pm \delta\theta$ are indicated as the solid green (online version only) areas of the cone surface. The fractional CE photon yield within $\theta \pm \delta\theta$ is equivalent to the fractional arc length $2\psi/2\pi$. The latter is related to charged particle energy and direction for a given step through the CE angle θ_{CE} [3] and the particle z direction cosine $\|\mathbf{w}\|$, respectively. The $2\psi/2\pi$ term is included in $\Phi_E^{\theta \pm \delta\theta}$ in Equation 1b and used to weight the CE power S_{CE} in scoring the $k_C^{\theta \pm \delta\theta}$ factor in the code.

The code outputs dose per incident fluence, as well as $k_C^{\theta \pm \delta\theta}$ as energy deposited per CE photon spectral density at $n = 1.34$ in units of $\text{MeV} \cdot \text{eV} \cdot \text{photon}^{-1}$. From this, we calculate CE photon spectral density per mass per incident fluence (under the same conditions). A thin-slab test was performed to ensure the modified code behaves correctly

in accordance with the CE theory.[3] This entailed simulating monoenergetic parallel electron beams of 0.1-50 MeV energies and 1-cm radius incident on a water slab of 10-cm radius and 1-pm width along the beam axis. The width was chosen to ensure that electrons traverse the thin slab without energy loss and in a straight line, so that their energy, path length, and direction are exactly known. This allows to calculate the theoretical CE photon spectral density per unit mass as the denominator of Equation 1b (using Equation 1c and normalizing by mass density) and the theoretical CE angle, $\cos\theta_{\text{CE}} = (n\beta)^{-1}$. [3, 14]

The considered $\theta \pm \delta\theta$ for the clinical electron beam simulation are $90^\circ \pm 90^\circ$ (4π detection), $90^\circ \pm 5^\circ$, and $42^\circ \pm 5^\circ$. The 42° angle is the CE angle of relativistic electrons in water,[3, 14] which constitute the bulk of the fluence spectrum, scatter the least, and have the highest CE power.[2] Therefore, the 42° configuration provides the highest signal within a constrained angular aperture. However, 42° relative to the surface tangent is also the angle of total internal reflection at a water-air interface[14] and, therefore, the detector must be placed in the water with conventional phantom geometries (e.g., cubic/cylindrical). Alternatively, reflection losses can be mitigated with a non-conventional phantom geometry. On the other hand, detection at 90° is simplest in terms of setup, allowing detector positioning in air with the use of a simple phantom as it entails minimal reflectance loss at a phantom exit surface that is parallel to the beam (such as for a cubic or a cylindrical phantom). Lastly, the 4π configuration may require 4π detection geometry or complete conversion to an isotropic signal with the use of a fluorophore as has been suggested in previous work.[25] This, however, would introduce additional uncertainty contributions of the fluorophore quantum yield, potential deviation from isotropic fluorescence, and scintillation contamination.[26] The CE scoring polar angle range $\theta \pm \delta\theta$ was added as an input to the modified SPRRZnrc code, with a default value of $90^\circ \pm 90^\circ$ (i.e., 4π detection).

Unless otherwise specified, the default EGSnrc transport parameters were used.[20] For the Monte Carlo validation study, the length of the scoring bins along the depth direction was 0.2 cm. Typically of the order of 10^7 - 10^8 histories were simulated at incidence (of the order of 1-10 CPU hours, Intel Xeon E5-2687W) to ensure dose uncertainty at d_{max} within 0.3%. To initiate future efforts towards detector development via optical design of a CE-based dosimeter, we also extended the code to score CE spectral and angular distributions.[3]

B. Experimental validation

Experiments were carried out on a Varian TrueBeam with nominal electron beam energies of 6, 12, and 20 MeV, at 90° detection, and with the setup shown in Figure 1. The beam was centered on a 30-cm^3 polycarbonate water tank with 6-mm walls filled with deionized water. We use a simple detector prototype, built in-house from a minimum number of components, including two spherical lenses and a multimode optical fiber, with a detection volume that is focused on beam axis and spans the water tank as indicated by the gray double cone in the water in Figure 1. This serves to also validate the Monte Carlo calculations in the penumbra region, which is included in the sensitive volume, and for angular variations about the 90° detection angle. In addition, by focusing the optics to the central beam axis, we take account of the lateral positioning uncertainty contribution of focusing on beam axis, as opposed to focusing away from beam axis or using an unfocused setup, e.g., a fiber without lenses.

The detector system was composed of a diffraction grating spectrometer (Shamrock 193i, SR2-GRT-0300-0500 grating, Andor Technology Ltd, Belfast, United Kingdom), with a pair of plano-convex spherical lenses (N-BK7, AR Coating: 350-700 nm, Thorlabs, Inc., Newton, NJ) focusing into a 15-m, high-OH, NA = 0.22, MFD = 0.1 mm optical

fiber input (93% transmittance at 500 nm, source: Thorlabs, Inc.), and a cooled to -80°C back-illuminated CCD (Newton EMCCD, 1600×200 , $16\ \mu\text{m}$ pixels, Andor Technology Ltd). To reduce readout noise, the full CCD chip was used and binned in the vertical direction (200 pixels) and, because CE is a broadband signal, the (horizontal) wavelength resolution was binned to 2 nm during readout. For the depth scan studies, spectra were binned from 400 nm to 600 nm during post-processing. A long fiber was used to allow positioning of the spectrometer and CCD outside the treatment room to avoid their irradiation. To minimize spherical aberration, the focusing optical assembly made use of a pair of plano-convex lenses oriented as in Figure 2 and the AA was limited with a pair of apertures adjacent and on the outside of the lens pair.[27] The focal point cross-section (perpendicular to the optical axis) in water was 0.5 mm with the largest AA ($\pm 2^{\circ}$). The optics were mounted on a cage system attached to a laser table, which was positioned on the couch for remote depth scanning and aligned with the treatment room lasers.

Optical alignment was achieved with a broadband LED source passed through the fiber (disconnected from the spectrometer) and optics in the reverse direction of CE detection. The fiber was positioned at the focal point of the focusing lens (i.e., the right lens in Figure 2, which focuses CE into the fiber) by checking collimation of the light source with that lens alone in air. The focal point in water together with the radiation beam were centered on the water phantom to ensure a symmetric measurement volume (and thus minimize its depth extent) by verifying that the AA diameters at the near and far tank walls were within 0.5 mm of each other. Depth positioning was achieved by aligning the light source image, shown in Figure 5, at the water surface in the far field, in a manner analogous to ionization-based dosimetry.[28]

Experiments were done with optical blackout material covering the entire setup to eliminate stray light, as well as on the far wall of the tank, as seen in Figure 1, to eliminate reflections. The background readings in the fiber and in the tank wall near the detector were acquired with the inside of the wall covered with blackout material. Depth CE was scanned remotely with the couch controls. Depth dose was scanned with an IBA CC13 ionization chamber. The purpose of the experimental validation is to make a first-order estimate of the uncertainty on the CE-to-dose conversion based on the difference between Monte Carlo and experiment. The results reported here are relative and could be improved and extended by use of diffraction-limited optics and absolute irradiance calibration of the detector system.

IV. RESULTS

A. Thin slab test of the Monte Carlo CE calculation framework

It was verified for monoenergetic parallel electrons in the 0.1-50 MeV energy range that the simulated CE photon spectral density per unit mass (calculated from dose and $k_C^{\theta \pm \delta\theta}$) and the simulated CE angle in a 1-pm thin slab of water are in agreement with theory[3, 14] to $\pm 0.03\%$ and $\pm 0.01^{\circ}$, respectively, within the simulation precision of 1×10^{-4} MeV / (photon/eV). The relative difference between the theoretically calculated and simulated CE spectral density scored within $\pm 0.01^{\circ}$ of the theoretically calculated CE polar angle is plotted in Figure 6 as a function of incident electron energy. It was also verified that the simulated CE spectral density at other angles is zero within the simulation precision.

B. Calculated $k_C^{\theta \pm \delta\theta}$ factors for electron beams from our clinical machine and detection angle optimization

The experimental validation with electron beams in Section IV C involves a comparison of calculated and measured CE depth scans within the large double cone sensitive volume indicated in gray in Figure 1 (Section III B). As will become evident below in Section IV D 2, the shape of the angular distribution is minimally affected by lateral integration of the sensitive volume. Therefore, since we are ultimately interested in the central-axis CE and k_C distributions, we take a closer look at them here and based on this we optimize the detection configuration for the experimental validation study that follows.

In Figures 7 and 8 we show representative simulation results of the electron beam percent-depth dose (PDD), percent-depth CE (PDC) generated in all directions (4π) and at polar angles of $90^\circ \pm 5^\circ$ and $42^\circ \pm 5^\circ$ relative to the beam axis, as well as the corresponding PDD-to-PDC ratios. The latter are equivalent to CE-to-dose conversion factors, $k_C^{\theta \pm \delta\theta}$, for $\theta \pm \delta\theta \in \{90^\circ \pm 90^\circ (4\pi), 90^\circ \pm 5^\circ, 42^\circ \pm 5^\circ\}$, normalized by the ratio of dose to CE maximum, which is provided in the legend.

C. Agreement of calculated and experimental relative $k_C^{90^\circ \pm 2^\circ}$ factors

In Figures 9 and 10, we show representative experimental and corresponding simulation results with two electron beam qualities of the PDD, PDC at 90° to the beam with 2° AA, as well as the corresponding PDD-to-PDC ratios, which are essentially normalized CE-to-dose conversion factors k_C . The locally-normalized difference between simulated and experimental relative k_C factors (i.e., PDD/PDC ratios), or equivalently between calculated PDD (as the product of the experimental PDC and the simulated relative k_C) and experimental PDD, is within 1% for PDC values higher than 50%. At shallow and large depths, the discrepancies are attributable to optical aberrations as well as reflections at the water-air interface.[14] This is discussed further in Section V.

D. Detection considerations at $\theta = 90^\circ$

1. CE spectrum

In Figure 11, we show simulated CE spectra in water and measured spectra at 90° to the beam for a range of electron beam qualities and depths, together with the Frank-Tamm equation for the CE spectrum of relativistic electrons ($\beta = 1$) in water.[2, 14] The difference between the measured and simulated spectra arises mainly from the detector system spectral sensitivity. As mentioned previously, we perform a relative experimental validation study of the Monte Carlo code in order to motivate detector development efforts. Therefore, as discussed below in Section V, the depth invariance of the CE spectrum observed in Figure 11 indicates that the spectral sensitivity is not relevant in the current context.

2. CE angular distribution

Simulated broad electron beam central-axis CE angular distributions at $n = 1.34$ in water[2, 3, 14] for a range of beam qualities and depths, normalized to their respective maxima, are shown in Figures 12a and 12b, normalized to solid angle and polar angle range $\delta\theta$, respectively. Normalization constants are also provided in terms of CE photons per unit CE energy bandwidth, solid angle or $\delta\theta$, mass, and incident fluence to allow the reader to estimate the optical power (typically in the pW-nW range) for a specific application. The length of the scoring voxels was 2 mm in the depth direction. Please note that these values are provisional, contingent on absolute experimental validation and optimization of the code. For comparison with a 6 MV photon beam study,[10] in Figure 12c the distributions are laterally averaged over a 100-cm radius water volume.

3. Angular aperture

Figure 13 shows simulation results at 90° detection with varying $\delta\theta$ for a 12 MeV beam as representative of both high and low beam energies. For illustrative purposes, the PDC is shown for $\pm 4^\circ$ variations in $\delta\theta$ about the $\theta \pm \delta\theta = 90^\circ \pm 5^\circ$ configuration. However, the $k_C^{\theta \pm \delta\theta}$ factor is non-linear with $\delta\theta$ variations. Therefore, to examine the dependence on small $\delta\theta$ variations, simulations were performed for $\pm 0.1^\circ$ variations about the $\theta \pm \delta\theta = 90^\circ \pm 5^\circ$ configuration. The locally-normalized difference, also shown in Figure 13, was found to be within $\pm 2.2\%$ at all depths and beam energies.

Figure 14 is the experimental equivalent of Figure 13 with AA of 2° (10-mm maximum aperture diameter at the tank wall) and 1° (5-mm maximum diameter). The 2° AA is the largest achievable with our setup and optics. The locally-normalized % difference in this case is calculated from the absolute background-subtracted and mass-normalized optical readings (counts/s per ray optics-approximated sensitive volume mass) at 1° and 2° AA and therefore corresponds to $\pm 0.5^\circ$ variation about the average AA (1.5°).

4. Robustness

The uncertainty contribution stemming from the robustness of the measurement system, calculated from two measurement sessions separated by 7 days and involving reassembly, refocusing, and re-collimation of the detector head, as well as changes in lens material and ± 1 cm changes in lens focal length and position, was found to be up to 1% ($k = 1$) at PDC values higher than 50%. The results of this study at 90° detection with 2° and 0° AA are shown in Figure 15.

The repeat measurement at 2° involved a switch from a 2-cm focal length ($f/2$) fused silica to a 5-cm focal length ($f/2$) N-BK7 focusing lens (right lens in Figure 1), as well as insertion of an aperture between the fiber and the focusing lens to limit the AA. The 0° measurement in Figure 15 involved the use of only a focusing lens. The repeat measurement at 0° involved decreasing the aperture diameter from 12 mm to 6 mm and normalizing by the corresponding volume ratio.

5. Background signal

There was no change in the CE background acquired by blacking out only the input optics instead of the inside face
 315 of the water tank wall near the detector, as described in Section III B, indicating that there is no CE contribution
 from the near wall. The CE background varied little in the z direction, which is characteristic of photon scatter, and
 it generally constituted up to 10% of the maximum raw signal with all energies depending on the aperture size and
 for couch shifts of the order of ± 1 cm. Variations in position and focal distance of the optics of 1 cm at constant
 couch position had no effect on the CE background, indicating that the background is mainly due to couch scatter.
 320 Contributions from the far-field wall of the water tank were estimated from measurements with and without blackout
 of the far wall and found to be up to $\sim 5\%$ of the local background-subtracted signal with all beam energies and
 characteristic of the electron PDC at 90° . This indicates that they are due to reflections of the in-field CE and not CE
 from the wall itself. To eliminate this effect, all measurements were done with blackout of the far wall as explained
 in Section III B. Finally, increasing the radius of curvature of the curved side of the lens by 1 cm, or equivalently the
 325 focal distance by 2.5 cm, of the collimating lens (i.e., the left lens in Figure 1) at constant (ray optics-approximated)
 sensitive volume increased the signal by up to 2% of the maximum, which indicates that optical aberrations result in
 contributions from points outside the sensitive volume.

V. DISCUSSION

With recent progress[6, 7, 29, 30] and increasing interest in the field for more than five years,[10] CE-based dosimetry
 330 is on its way to the clinic. However, a clinically-implementable CE-based dosimetry protocol has not been established.
 Accurate CE-to-dose conversion factors have not yet been made available. Furthermore, a high-resolution CE-based
 dosimeter of demonstrated sufficient accuracy has yet to be designed. In this work, we provide necessary means to
 move the field further forward. In comparison with ionization-based dosimetry,[8, 13] the sensitive volume in CE-
 based dosimetry is water and resolutions of the order of micrometers may potentially be achievable, contingent on a
 335 detector development study.[4, 5, 27] The absolute versus relative CE-based dosimetry endpoint is a matter of further
 investigation and also requires detector development. Here we motivate this by considering, from first principles,
 a potential broad-beam central-axis CE-based dosimetry formalism applicable to both photon and electron beams,
 developing an EGSnrc[9] simulation framework for the calculation of the CE-to-dose conversion, and performing a
 relative experimental validation and feasibility study in water using a simple detector and with electron beams for
 340 which the relative conversion is more sensitive to depth, beam quality, and angle than for photon beams.[7, 10, 11]
 Although CE-based dosimetry might ultimately provide solutions to the challenges faced by ionization chambers in a
 different clinical situation, e.g., small fields and MR-linacs, we begin the investigation with a look into the broad-beam
 CE-to-dose conversion on beam axis in water.

Because CE is anisotropic,[3] we first investigate potential detection configurations for the experimental validation
 345 study with electron beams. In Figures 7 and 8, we see that the electron beam central-axis PDC generated in 4π is
 upstream of the PDD. This is a consequence of the CE threshold energy[2] and is in agreement with Glaser et al.
 2014[7] and Helo et al. 2014,[6] where the Geant4-calculated[31] PDC generated in 4π was compared with the PDD
 of 6 and 9 MeV electron beams. A quantitative justification is provided in the companion Paper II, which is focused

solely on electrons beams.[12] As a result, the CE-to-dose conversion is beam quality and depth dependent. The
 350 implications of this on CE-based electron beam dosimetry are also discussed in Paper II.

In contrast to the central-axis PDC generated in 4π , the PDC at polar angles of $\theta \pm \delta\theta$ for small $\delta\theta$ depends not
 only on the charged particle fluence, but also on the scattering state of the beam due to the anisotropy of CE.[3]
 Therefore, as can be seen for electron beams in Figures 7 and 8, the PDC at $90^\circ \pm 5^\circ$ to the beam exhibits a steeper
 build-up, in agreement with Helo et al. 2014[6] for 6-12 MeV electrons, and is peaked at a larger depth than the 4π
 355 PDC, while the PDC at the 42° CE angle of relativistic electrons[3, 14] is peaked at $z = 0$ cm and decreases drastically
 away from the surface as electrons lose energy and become less forward-directed. Therefore, although it provides a
 strong signal within a constrained angular aperture,[2] the 42° configuration is impractical for dosimetric purposes as
 it not only requires in-water detector placement, or conversely a non-conventional phantom geometry, to correct for
 total internal reflection at the phantom wall,[14] but also normalization at $z = 0$ cm, which makes the measurement
 360 dependent on the size of the scoring volume. This in turn leads to a high uncertainty in the PDC-derived electron
 beam quality specifier, e.g., R_{50} [8] derived from the depth of 50% CE (discussed in Paper II).[12] Furthermore, at 42°
 we expect a high contribution from both depth and beam quality uncertainties due to the strong variation of $k_C^{42^\circ \pm \delta\theta}$
 with depth and beam quality for small $\delta\theta$.

The 90° configuration, on the other hand, appears to be the most practicable of the three because it allows in-air
 365 detector positioning with minimal reflectance losses with conventional phantoms. However, although $90^\circ \pm \delta\theta$ for small
 $\delta\theta$ is less susceptible to depth positioning uncertainties for CE-based dosimetry performed at a reference depth near
 d_{\max} , it exhibits beam quality dependence of the same order as 42° and it is very depth-sensitive near the surface. With
 a 4π configuration, the beam quality and depth dependence is greatly reduced; however, a 4π detection geometry is
 required. This could potentially be achieved in water, e.g., via tomographic reconstruction or with a small integrating
 370 sphere positioned on beam axis. The latter will, however, diminish the value of CE-based dosimetry as a perturbation-
 free technique. A more practical approach may employ an objective with a large numerical aperture and definition of
 the sensitive volume by means of a de-blurring technique, such as nearest neighbor.[5] Larger numerical apertures are
 considered in Paper II.[12] For broad photon beams in water, these effects are less pronounced[7, 10, 11] due to the
 existence of transient charged particle equilibrium (i.e., less variation of the charged particle fluence spectrum and
 375 angular distribution with depth). The experimental validation and feasibility here is performed with electron beams
 in water at 90° with AA of up to 2° .

As mentioned in Section II, the CE-based formalism involves CE detection with narrow response centered on the
 beam axis.[4] In our experiments, the response is broadened largely due to the use of simple spherical lenses and
 a multimode fiber-optic input. In the experimental analysis, we therefore assume a uniform response across the
 380 entire ray optics-approximated acceptance volume in water (the solid gray double cone in the water tank in Figure 1)
 and compare with Monte Carlo depth scans of CE scored within this large volume. In Section IV C, the dosimetric
 uncertainty contribution of the electron beam CE-to-dose conversion due to the difference between Monte Carlo-
 calculated and experimental PDD-to-PDC ratios is estimated at 1% to first order at depths where the PDC is $> 50\%$.
 This excludes the contribution from absolute calibration of the CE-based dosimeter, which is a matter of further
 385 investigation. This is an improvement from Helo et al. 2014,[6] where a ruler was used for depth positioning and
 camera magnification was shown to have a significant effect. At shallow and large depths, the discrepancies observed
 between the measured and Monte Carlo-calculated PDD-to-PDC ratios are attributable to optical aberrations and

reflections at the water surface where the angle of total internal reflection is 48° with respect to the surface normal.[14] Because the point of interest is on the optical axis (see Figure 2), the major aberrations at play are chromatic and spherical.[4] Off-axis aberrations likely also play a minor role, because a broad radiation beam (see Section III) results in a spatially broad CE signal (an extended light source). Due to spherical aberration, marginal rays that are focused into the optical fiber originate from points on the optical axis closer to the optics than the point of best focus, while paraxial rays originate from points further away.[4] Therefore, because the point of best focus was centered on the radiation beam central axis, as explained in Section III, spherical aberration increases the contribution of points lateral to the beam axis. At these lateral positions, the PDC at 90° is larger in the build-up and photon tail, which was also observed to be the case in our simulations.

The excellent agreement with the analytical Frank-Tamm spectrum[2] as well as the lack of variation with beam quality and depth observed in both simulation and experiment in Figure 11 serve as further validation of our EGSnrc CE calculation framework.[9, 20, 23] The CE spectrum of high-energy electron beams is independent of the electron fluence spectrum since the electron energy dependence stems from the $1/\beta^2$ term (see Equation 1c), which is slowly varying at relativistic energies.[2] The dose-CE relationship is therefore largely determined by the total fluence. This finding will facilitate detector design by relaxing the detector spectral response requirements. Furthermore, because the results of the experimental validation study of Section IV C are relative and because the CE spectrum is depth-invariant, the system quantum efficiency and spectral sensitivity are not required for this part of the work.

Because the CE angle is a function of $1/\beta$,[3] which is slowly varying at high energies, the CE angular distribution of high-energy beams is largely determined by the angular distribution of the charged particles and not by their energies. Due to scattering, in Figure 12 we therefore observe a strong variation of the simulated electron beam CE angular distribution with beam quality and depth, with a narrower distribution at high beam qualities and shallow depths peaked at the 42° CE angle of relativistic electrons in water[3, 14] and a shift of the peak towards higher θ with increasing depths in 12b. In comparing Figure 12c with a corresponding 6 MV photon beam study,[10] we see that, as expected, due to transient charged particle equilibrium, the photon beam CE angular distribution is much less depth-dependent. Note that 90° detection may not be optimal in terms of signal intensity. As we have shown in this study, however, CE by high-energy electron beams is readily detectable at 90° , even at superficial depths. Although this appears not to be the case in Figure 12a, this is an effect of normalization. In fact, the distribution with the lowest normalized value at 90° (20 MeV, 1 mm) corresponds to 50% of the absolute CE power of the distribution with the highest normalized value (6 MeV, R_{50}). At all depths and energies shown, the CE power at 90° , integrated over a 400-600 nm optical bandwidth, within an optical AA of $\pm 5^\circ$, in a 1 cm^3 volume of water, and at a dose rate of 400 MU/min is of the order of 1-10 pW.

It is also evident in Figure 12a that 90° detection is less sensitive to angle variations than detection near 42° and, in Figure 13, we further show that the simulated PDC at $90^\circ \pm 5^\circ$ is relatively insensitive to $\pm 4^\circ$ variation in $\delta\theta$. The 0.5-mm upstream shift with a $\delta\theta$ increase from 1° to 9° is due to an increasing contribution from electrons of higher energies, which are more forward-directed (see Equation 1c). The locally-normalized absolute CE (per mass) variation for $\pm 0.1^\circ$ variations about the $\theta \pm \delta\theta = 90^\circ \pm 5^\circ$ configuration was found to be within $\pm 2.2\%$ at all depths and beam energies. This corresponds to a relative standard uncertainty component (rectangular distribution) of $< 1.3\%$ ($k = 1$). This was also confirmed experimentally in Figure 14, where a $\pm 10\%$ variation in the mass-normalized optical readings was observed on average per $\pm 0.5^\circ$ variation in the optics AA. However, manufacturers (e.g., Edmund Optics Ltd)[32]

achievable angle tolerances of the order of arcseconds ($< 0.01^\circ$), which would bring the corresponding uncertainty down to $< 0.1\%$. Furthermore, for relative CE-based dosimetry, the relevant uncertainty is that of the PDC, which was found to be $< 0.1\%$ for $\delta\theta$ variations of 0.1° .

In Figure 15, we further demonstrate $\leq 1\%$ ($k = 1$) uncertainty contribution of the robustness of our provisional detector design (Figure 1) for PDC $> 50\%$ to reassembly, refocusing, collimation, lens material composition, and ± 1 cm changes in the focusing lens position and focal length (i.e., ± 0.5 cm changes in the convex radius of curvature of the right lens in Figure 1). The switch from a 2-cm to 5-cm focal length plano-convex focusing lens (f/2) and insertion of an aperture between the fiber and focusing lens to limit the 2° AA in Figure 15 is expected to reduce optical aberrations due to the decreased curvature of the 5-cm lens and restriction of the marginal acceptance by the aperture.[27] The agreement between the 2° curves in Figure 15, however, indicates that the effectiveness of these changes in reducing the aberrations is minor with this setup. The aberrations are expected to be minimized with detection optics optimization through modeling using diffraction-limited optics. An effort was made in this study to minimize the aberrations by use of two plano-convex lenses oriented as in Figure 2 and apertures on both sides of the lens assembly (see Section III B). In addition, the lack of observable volume averaging differences with the two apertures (12 versus 6 mm) at 0° in Figure 15 may be due to weighting of the optics acceptance towards the optical axis or to changes in the aberrations as a result of stopping down. On the other hand, volume averaging is evident in comparing the PDC curves with 0° versus 2° AA.

Background contributions to the measurements from points outside the (ray optics-approximated) sensitive volume in the water were also evaluated in Section IV D 5. The background signal was found to be mainly due to couch scatter entering the optics (fiber/lenses) and generating CE within the optics themselves. This is because the background signal was (1) characteristic of photon scatter, (2) strongly dependent on the longitudinal couch position for the same numerical aperture, and (3) independent of the longitudinal position of the optics for the same couch position and numerical aperture. In addition, CE contributions from the water tank wall near the detector (see Figure 1) were negligible, while contributions from the far-field wall constituted up to $\sim 5\%$ of the local background-subtracted signal and were due to reflections. Therefore, while the background signal (generated in the fiber and optics) with this setup can be acquired by closing the detector end aperture, we recommend blacking out the far wall. Finally, background contributions from points outside the ray optics-approximated sensitive volume, due to optical aberrations, were shown to increase by up to 2% of the maximum CE reading per 1 cm increase in the radius of curvature of the curved (non-plano) side of the collimating lens (i.e., the left lens in Figure 1).

In place of the 2D imaging systems used in the literature to detect CE in water,[6, 10, 11] we use a pair of plano-convex lenses with apertures focused on beam axis and feeding into a single long multimode fiber optic cable, leading to a spectrometer outside the treatment room (see Figure 1). This is motivated by the fact that it is a simple detector, individual optical components can be readily modified and reassembled, and more importantly it can be easily modeled and allows for a more direct comparison between Monte Carlo and experiment. There is no image distortion, vignetting,[6] or varying acceptance angles with depth.[10] With the exception of superficial measurements, the sensitive volume is constant with depth within the experimental uncertainties. In addition, the use of a spectrometer provides spectral measurements (Section IV D 1) and its positioning outside of the treatment room eliminates scatter radiation noise.[6] This setup can be extended to 2D by use of lens and fiber arrays in combination with a multi-channel spectrometer.

A limitation of our detector design is the use of spherical lenses, which nevertheless made possible the evaluation of the effect of optical aberrations (Sections [IV D 4](#) and [IV D 5](#)). In addition, the response spanned the entire water tank (Figure 1) and our results are relative. As discussed throughout, this work aims to motivate optical design and characterization of a CE-based dosimeter with narrow response on beam axis, which requires further investigation and may potentially involve optical sectioning techniques[5] or 4π detection via, e.g., tomographic reconstruction combining projections from non-parallel sets of planes. CE detector optical design, absolute irradiance calibration, and characterization will allow evaluation of detector-related uncertainties specific to CE-based dosimetry and comparison with current practice in reference and relative dosimetry. CE may be especially promising for small-field dosimetry[33] due to the small resolutions achievable via, e.g., optical sectioning techniques.[5]

A limitation of the formalism outlined in Section II is the beam quality and depth dependence of the CE-to-dose conversion. We take an in-depth look at the corresponding uncertainty contributions to CE-based electron beam dosimetry in Paper II.[12] For photon beams, weaker overall dependencies are expected as discussed throughout this work and observed in the literature.[7, 10, 11] These limitations pave important venues to be explored in the future efforts towards full clinical implementation of CE-based dosimetry.

VI. CONCLUSIONS

CE-based dosimetry of both large and small-field external radiotherapy beams has received much attention over the last decade as it carries promise as an in-water perturbation-free high-resolution technique. That is, it involves detection of CE from the beam directly in water with a detector positioned out of the beam at resolutions potentially of the order of micrometers. In this study, we consider a broad-beam central-axis CE-to-dose conversion formalism, modify the SPRRZnrc Monte Carlo code for calculation of the conversion, and carry out relative experimental validation of the code with a simple detector in electron beams. Photon beams are expected to be less sensitive to experimental uncertainties and this is confirmed by comparison with the literature. Electron beam CE-based dosimetric uncertainties related to the CE-to-dose conversion are addressed in greater detail in a companion study. The aim of the current study is to motivate detector development and characterization of a CE-based dosimeter and phantom system, which is envisioned to employ optical sectioning or tomographic techniques and will make possible evaluation of the detector-related uncertainties specific to CE-based dosimetry in relation to specific applications in current practice. CE may carry promise as a small-field technique due to the small resolutions achievable in optical imaging.

ACKNOWLEDGMENTS

The authors would like to thank Joe Larkin of the McGill University Health Centre for help with the construction of the experimental setup, Francois Therriault-Proulx of Centre Hospitalier Universitaire de Montréal for valuable discussions on optical instrumentation, and Marc-André Renaud for help with setting up the simulations. YZ acknowledges partial support by the CREATE Medical Physics Research Training Network grant of the Natural Sciences and Engineering Research Council (NSERC) (#432290), CREATE - Integrated Sensor Systems grant of NSERC (#371305), and Bourses de doctorat en recherche (B2) du Fonds de recherche du Québec - Nature et technologies (FRQNT) (#184385). This work was partially supported by NSERC (#RGPIN-2014-06475, #231909).

VII. DISCLOSURE OF CONFLICTS OF INTEREST

The authors have no conflicts to disclose.

-
- [1] P. Cherenkov, "Vidimoe svechenie chistykh zhidkostei pod deistviem gamma-radiatsii" (Visible glow of pure liquids under gamma radiation), Dokl. Akad. Nauk SSSR **2**, 451–457 (1934).
- 505 [2] I. Tamm and I. Frank, "Kogerentnoe izluchenie bystrogo elektrona v srede" (Coherent radiation of a fast electron in a medium), Dokl. Akad. Nauk **14**, 107–112 (1937).
- [3] J. V. Jelley, Čerenkov radiation and its applications, British Journal of Applied Physics **6**, 227–232 (1955).
- [4] D. Malacara-Hernández and Z. Malacara-Hernández, *Handbook of Optical Design, Third Ed.*, CRC Press, 2014.
- 510 [5] D. A. Agard, Y. Hiraoka, P. Shaw, and J. W. Sedat, Chapter 13: Fluorescence Microscopy in Three Dimensions, in *Fluorescence Microscopy of Living Cells in Culture Part B. Quantitative Fluorescence Microscopy-Imaging and Spectroscopy*, edited by D. L. Taylor and Y.-L. Wang, volume 30 of *Methods in Cell Biology*, pages 353 – 377, Academic Press, 1989.
- [6] Y. Helo, I. Rosenberg, D. D'Souza, L. MacDonald, R. Speller, G. Royle, and A. Gibson, Imaging Čerenkov emission as a quality assurance tool in electron radiotherapy, Phys Med Biol **59**, 1963–1978 (2014).
- 515 [7] A. K. Glaser, R. Zhang, D. J. Gladstone, and B. W. Pogue, Optical dosimetry of radiotherapy beams using Čerenkov radiation: the relationship between light emission and dose, Phys Med Biol **59**, 3789–3811 (2014).
- [8] P. R. Almond, P. J. Biggs, B. M. Coursey, W. F. Hanson, M. S. Huq, R. Nath, and D. W. O. Rogers, AAPM's TG-51 protocol for clinical reference dosimetry of high-energy photon and electron beams, Med Phys **26**, 1847–1870 (1999).
- [9] I. Kawrakow, Accurate condensed history Monte Carlo simulation of electron transport. I. EGSnrc, the new EGS4 version, Med Phys **27**, 485–498 (2000).
- 520 [10] A. K. Glaser, S. C. Davis, D. M. McClatchy, R. Zhang, B. W. Pogue, and D. J. Gladstone, Projection imaging of photon beams by the Čerenkov effect, Med Phys **40**, 012101–1–012101–13 (2013).
- [11] A. K. Glaser, W. H. A. Voigt, S. C. Davis, R. Zhang, D. J. Gladstone, and B. W. Pogue, Three-dimensional Čerenkov tomography of energy deposition from ionizing radiation beams, Opt. Lett. **38**, 634–636 (2013).
- 525 [12] Y. Zlateva, B. Muir, J. Seuntjens, and I. El Naqa, Čerenkov emission-based external radiotherapy dosimetry: II. Electron beam quality specification and uncertainties, Med Phys (submitted).
- [13] P. Andreo, D. Burns, K. Hohlfield, M. Huq, T. Kanai, F. Laitano, V. Smyth, and S. Vynckier, Absorbed Dose Determination in External Beam Radiotherapy, Technical Report Series 398, International Atomic Energy Agency, Vienna, 2000.
- [14] M. Daimon and A. Masumura, Measurement of the refractive index of distilled water from the near-infrared region to the ultraviolet region, Appl. Opt. **46**, 3811–3820 (2007).
- 530 [15] L. V. Spencer and F. H. Attix, A Theory of Cavity Ionization, Radiation Research **3**, 239–254 (1955).
- [16] M. McEwen, L. DeWerd, G. Ibbott, D. Followill, D. W. O. Rogers, S. Seltzer, and J. Seuntjens, Addendum to the AAPM's TG-51 protocol for clinical reference dosimetry of high-energy photon beams, Med Phys **41**, 041501–1–041501–20 (2014), 041501.
- 535 [17] Key Data for Ionizing-Radiation Dosimetry: Measurement Standards and Applications, Technical Report 90, International Commission on Radiation Units and Measurements, 2014.
- [18] D. W. O. Rogers, B. A. Faddegon, G. X. Ding, C.-M. Ma, J. We, and T. R. Mackie, BEAM: A Monte Carlo code to simulate radiotherapy treatment units, Med Phys **22**, 503–524 (1995).
- [19] D. Rogers, B. Walters, and I. Kawrakow, BEAMnrc Users Manual, Technical Report PIRS-0509(A)revL, National Research Council of Canada, Ottawa, Canada, 2012.

- 540 [20] I. Kawrakow, E. Mainegra-Hing, D. Rogers, F. Tessier, and B. Walters, The EGSnrc Code System: Monte Carlo Simulation of Electron and Photon Transport, Technical Report PIRS-701, National Research Council of Canada, Ottawa, Canada, 2011.
- [21] A. Rodrigues, D. Sawkey, F.-F. Yin, and Q. Wu, A Monte Carlo simulation framework for electron beam dose calculations using Varian phase space files for TrueBeam Linacs, *Med Phys* **42**, 2389–2403 (2015).
- 545 [22] <https://github.com/yanazlateva/scrrznrc/tree/f5356f63166a538ebd3b8f84775b5de69e895428>.
- [23] D. Rogers, I. Kawrakow, J. Seuntjens, B. Walters, and E. Mainegra-Hing, NRC User Codes for EGSnrc, Technical Report PIRS-702(RevB), National Research Council of Canada, Ottawa, Canada, 2003.
- [24] G. M. Hale and M. R. Querry, Optical Constants of Water in the 200-nm to 200- μ m Wavelength Region, *Appl. Opt.* **12**, 555–563 (1973).
- 550 [25] A. K. Glaser, S. C. Davis, W. H. A. Voigt, R. Zhang, B. W. Pogue, and D. J. Gladstone, Projection imaging of photon beams using Čerenkov-excited fluorescence, *Phys Med Biol* **58**, 601–619 (2013).
- [26] E. Jean, M.-E. Delage, and L. Beaulieu, Investigation of the quinine sulfate dihydrate spectral properties and its effects on Cherenkov dosimetry, arXiv preprint arXiv:1809.02048 (2018).
- [27] W. Smith, The Primary Aberrations, in *Modern Optical Engineering, 4th Ed.*, McGraw Hill professional, chapter 5, McGraw-Hill Education, 2007.
- 555 [28] I. J. Das, C.-W. Cheng, R. J. Watts, A. Ahnesjö, J. Gibbons, X. A. Li, J. Lowenstein, R. K. Mitra, W. E. Simon, and T. C. Zhu, Accelerator beam data commissioning equipment and procedures: Report of the TG-106 of the Therapy Physics Committee of the AAPM, *Med Phys* **35**, 4186–4215.
- [29] A. Glaser, J. Andreozzi, R. Zhang, B. W Pogue, and D. J Gladstone, Optical cone beam tomography of Cherenkov-mediated signals for fast 3D dosimetry of X-ray photon beams in water, *Med Phys* **42**, 4127–4136 (2015).
- 560 [30] P. Bruza, J. M. Andreozzi, D. J. Gladstone, L. A. Jarvis, J. Rottmann, and B. W. Pogue, Online Combination of EPID & Cherenkov Imaging for 3-D Dosimetry in a Liquid Phantom, *IEEE Transactions on Medical Imaging* **36**, 2099–2103 (2017).
- [31] S. Agostinelli et al., Geant4-a simulation toolkit, *Nuclear Instruments and Methods in Physics Research Section A: Accelerators, Spectrometers, Detectors and Associated Equipment* **506**, 250 – 303 (2003).
- 565 [32] Edmund Optics Inc., Understanding Optical Specifications, <https://www.edmundoptics.com/resources/application-notes/optics/understanding-optical-specifications/>, 2018, Accessed on 2018-10-20.
- [33] F. Crop, N. Reynaert, G. Pittomvils, L. Paelinck, C. D. Wagter, L. Vakaet, and H. Thierens, The influence of small field sizes, penumbra, spot size and measurement depth on perturbation factors for microionization chambers, *Phys Med Biol* 570 **54**, 2951–2969 (2009).

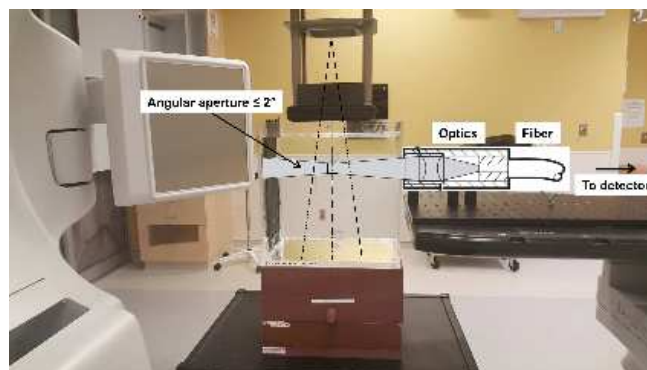


FIG. 1. Experimental setup for the detection of Cherenkov emission in water. Diagram is not to scale.

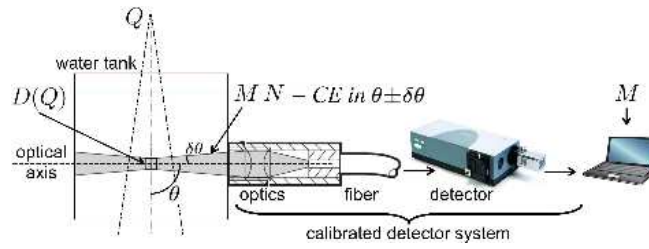


FIG. 2. Schematic of Cherenkov emission (CE) detection setup for CE-based dosimetry of external radiotherapy beams, with variables defined in Equation 1. Diagram is not to scale.

FIG. 3. Cherenkov emission (CE) power (Equation 1c with $n = 1.34$) and unrestricted collision stopping power (right y-axis, dashed line) as functions of electron kinetic energy in the range 0.1-10 MeV in water.[2, 14, 17]

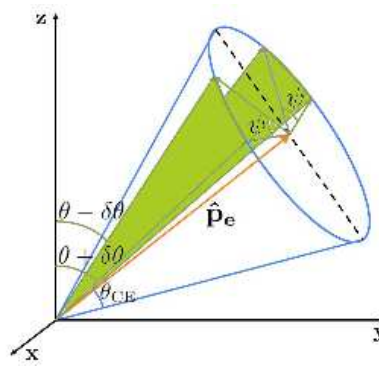


FIG. 4. (b) Sample geometry for scoring the fraction, $2\psi/2\pi$, of CE photons generated by an electron of momentum unit vector $\hat{\mathbf{p}}_e$ (corresponding to CE cone angle θ_{CE}) that fall within the detection angle range of $\theta \pm \delta\theta$. Note that the axes are rotated 180° with respect to the x-axis in Figure 2 to facilitate visualization.

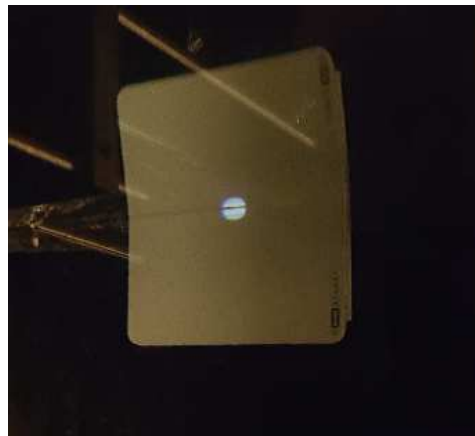


FIG. 5. Image of the light circle formed in the far field at the water tank surface by an LED source illuminating the detector end of the optical fiber in Figure 1. The camera is positioned outside the tank and below the surface.

FIG. 6. Relative difference between theoretical and Monte Carlo-calculated Cherenkov emission (CE) photon spectral density generated at the theoretically calculated CE angle[3, 14] $\pm 0.01^\circ$ in a thin water slab in terms of incident electron energy.

FIG. 7. Simulated (a) percent-depth dose, PDD, percent-depth Cherenkov emission, $PDC^{\theta \pm \delta\theta}$, and (b) normalized Cherenkov-to-dose conversion factors, $k_C^{\theta \pm \delta\theta}$, in water, at polar angles $\theta \pm \delta\theta$ of $90^\circ \pm 90^\circ$ (4π), $90^\circ \pm 5^\circ$, and $42^\circ \pm 5^\circ$ relative to the beam, for a TrueBeam 6 MeV electron beam.

FIG. 8. Same as Figure 7 but for TrueBeam 22 MeV electrons.

FIG. 9. (a) Simulated (Sim) and experimental (Exp) percent-depth dose, PDD, percent-depth Cherenkov emission, PDC, at 90° to the beam with $\pm 2^\circ$ angular aperture, and (b) corresponding PDD-to-PDC ratios, representing normalized Cherenkov-to-dose conversion factors, k_C , and their locally-normalized % difference, in water for a TrueBeam 6 MeV electron beam, using the setup of Figure 1. The error bars define an interval estimated to have 95% level of confidence, based on the t-distribution for 4 degrees of freedom (5 acquisitions) and calculated solely from the experimental standard deviation of the mean background-subtracted optical reading at each depth.

FIG. 10. Same as Figure 9 but for TrueBeam 20 MeV electrons.

FIG. 11. Simulated CE and measured spectra at 90° to the beam of TrueBeam 6 and 20 MeV electron beams at various depths in water. The Frank-Tamm equation for relativistic electrons ($\beta = 1$) is also shown for reference.[2, 3]

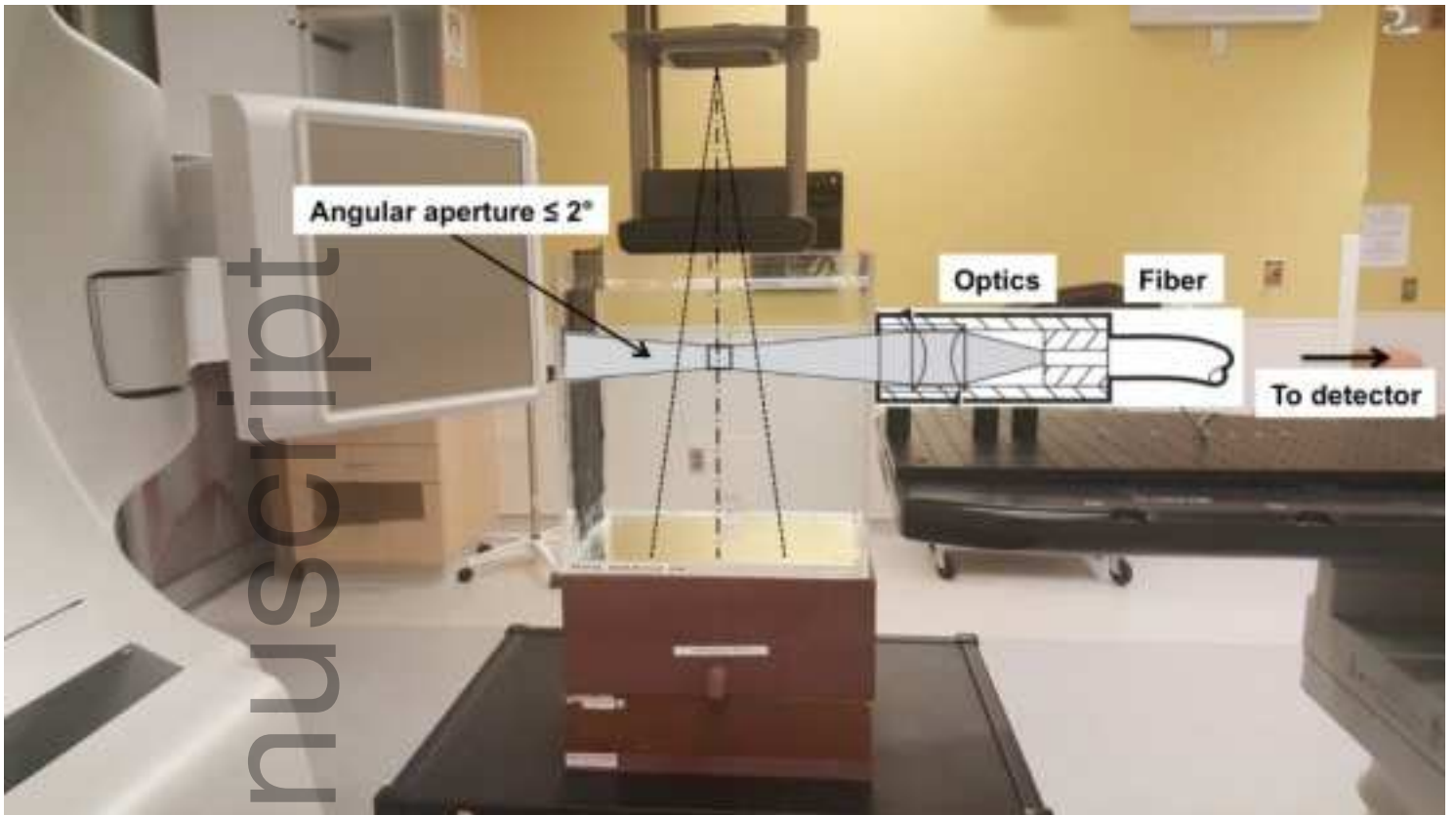
(a)
(b)
(c)

FIG. 12. (a) Simulated broad-beam central-axis CE angular distributions of TrueBeam 6 and 20 MeV electron beams at $n=1.34$ in water[2, 3, 14] at various depths. Normalization constants are shown in terms of CE photons per unit CE energy bandwidth, solid angle, mass, and incident fluence. (b) The CE angular distributions of (a) per unit polar angle instead of solid angle (i.e., azimuthally integrated). (c) The CE angular distributions of (b), but integrated over 100-cm water radius.

FIG. 13. Simulated (a) percent-depth dose, PDD, percent-depth Cherenkov emission (CE), $PDC^{\theta \pm \delta\theta}$, at polar angles $\theta \pm \delta\theta$ of $90^\circ \pm 90^\circ$ (4π), $90^\circ \pm 9^\circ$, and $90^\circ \pm 1^\circ$ relative to the beam, and (b) corresponding normalized CE-to-dose conversion factors, $k_C^{\theta \pm \delta\theta}$, and locally-normalized % difference on absolute CE values corresponding to $\delta\theta$ variations of $\pm 0.1^\circ$ about 5° , in water for a TrueBeam 12 MeV electron beam.

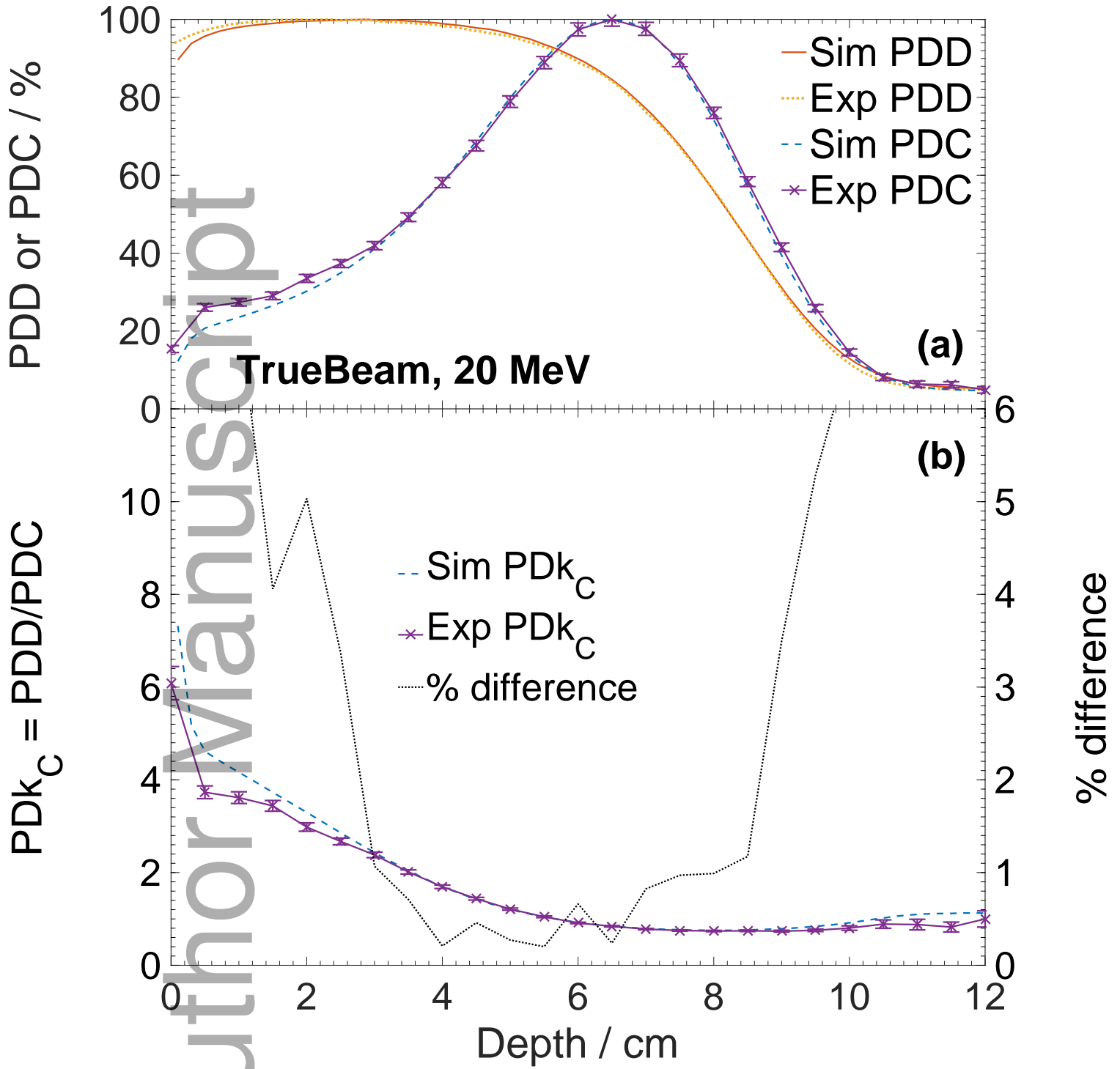
FIG. 14. Experimental equivalent of Figure 13 but for optical angular aperture (AA) of 2° and 1° and corresponding locally-normalized % difference on the absolute background-subtracted and mass-normalized optical readings (counts/s per ray optics-approximated sensitive volume mass). The error bars are computed as in Figure 9.

FIG. 15. (a) Experimental Cherenkov emission (CE) reading at 90° to the beam from repeat measurements at 2° and 0° angular aperture with optics reassembly, refocusing, and slight change of setup (namely, focusing lens shape for 2° and collimation for both 2° and 0°). The reproduced 0° curve (repr, $90^\circ \pm 0^\circ$) is volume-ratio normalized to account for aperture differences between the two experiments. (b) Corresponding averaged percent-depth CE, PDC, at 90° to the beam (error bars are not computed as they have no relevance to the discussion) and robustness, represented as relative standard uncertainty ($k = 1$). These results are for CE measurements in water from a TrueBeam 12 MeV electron beam, using the setup of Figure 1. The error bars are computed as in Figure 9.

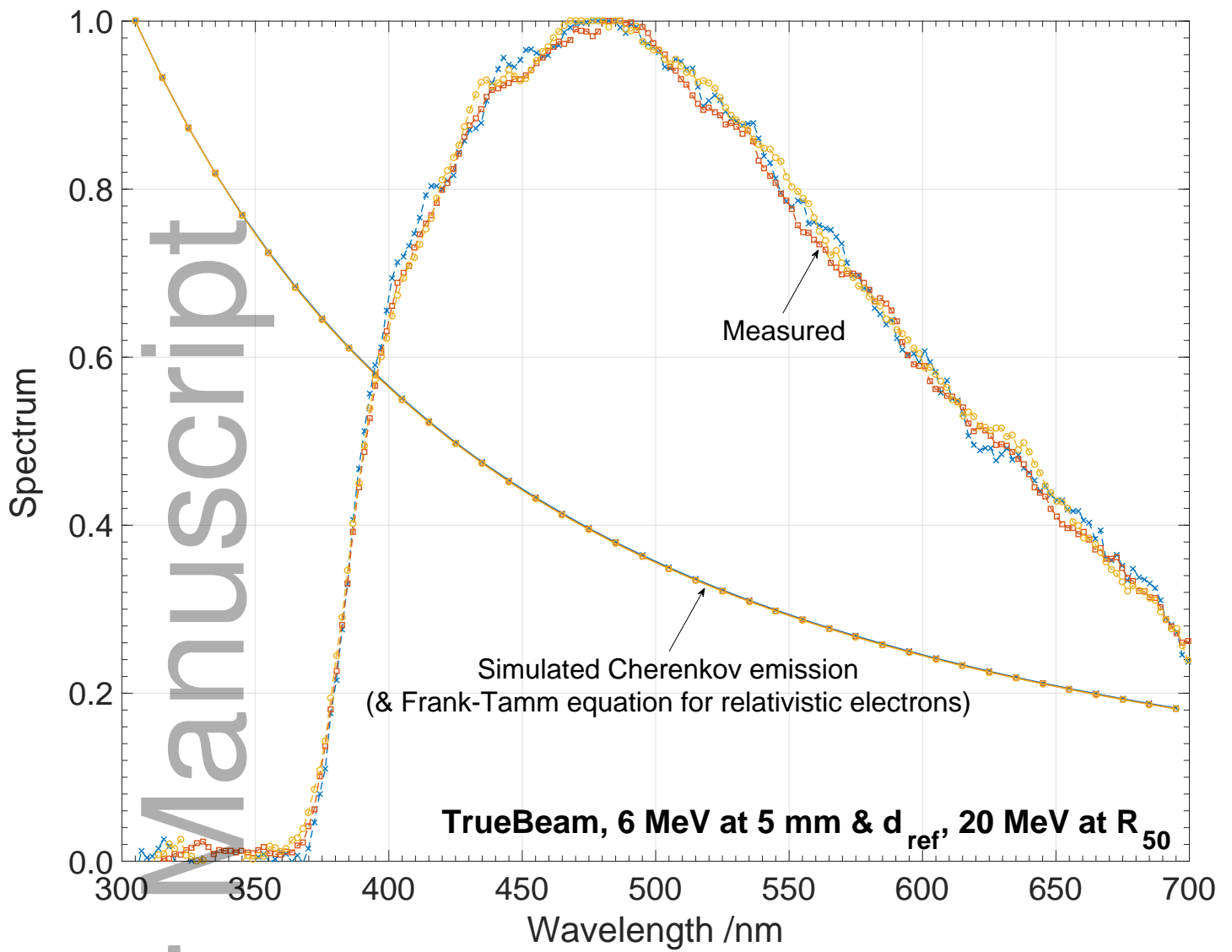


mp_13414_f1.jpg

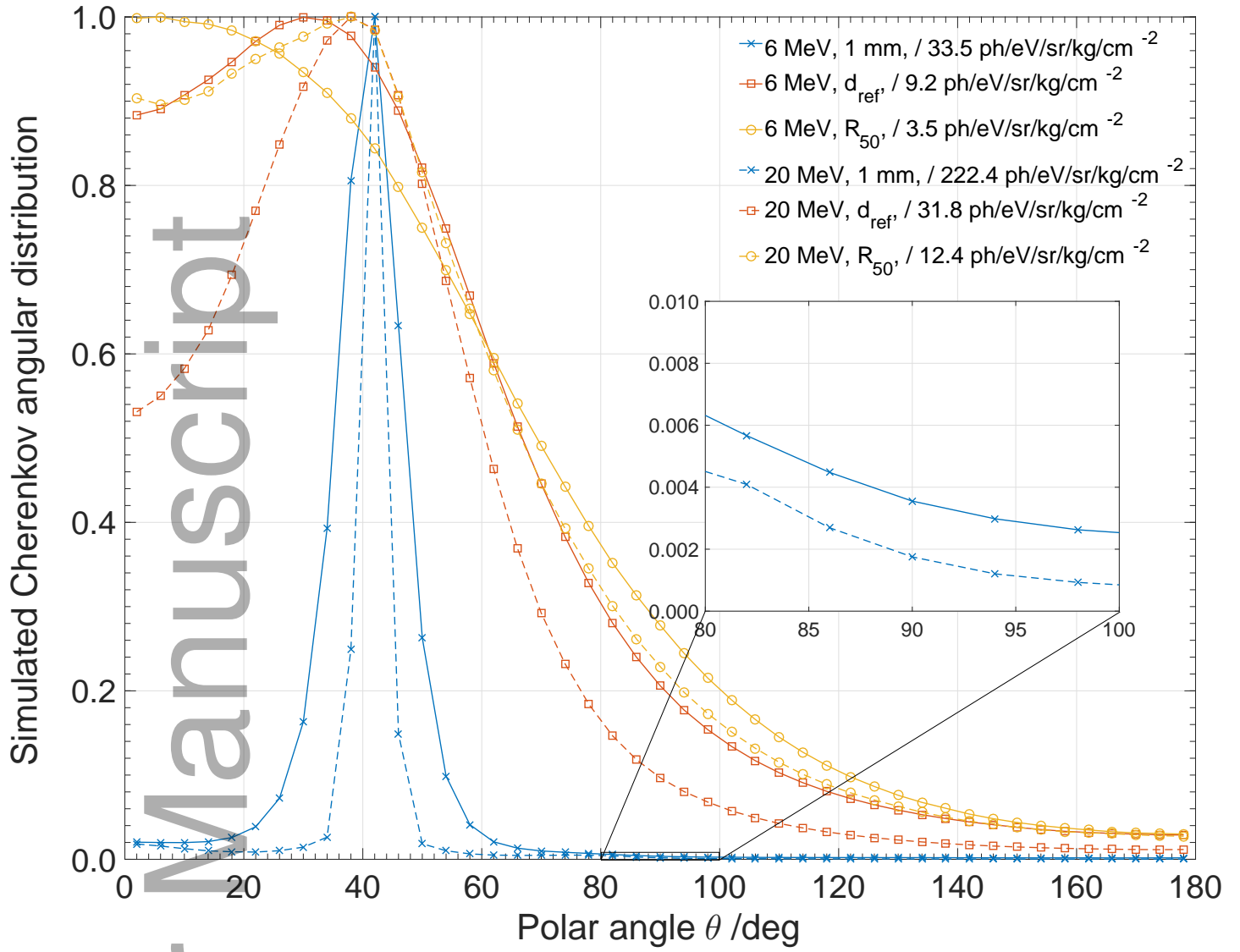
Author Manuscript

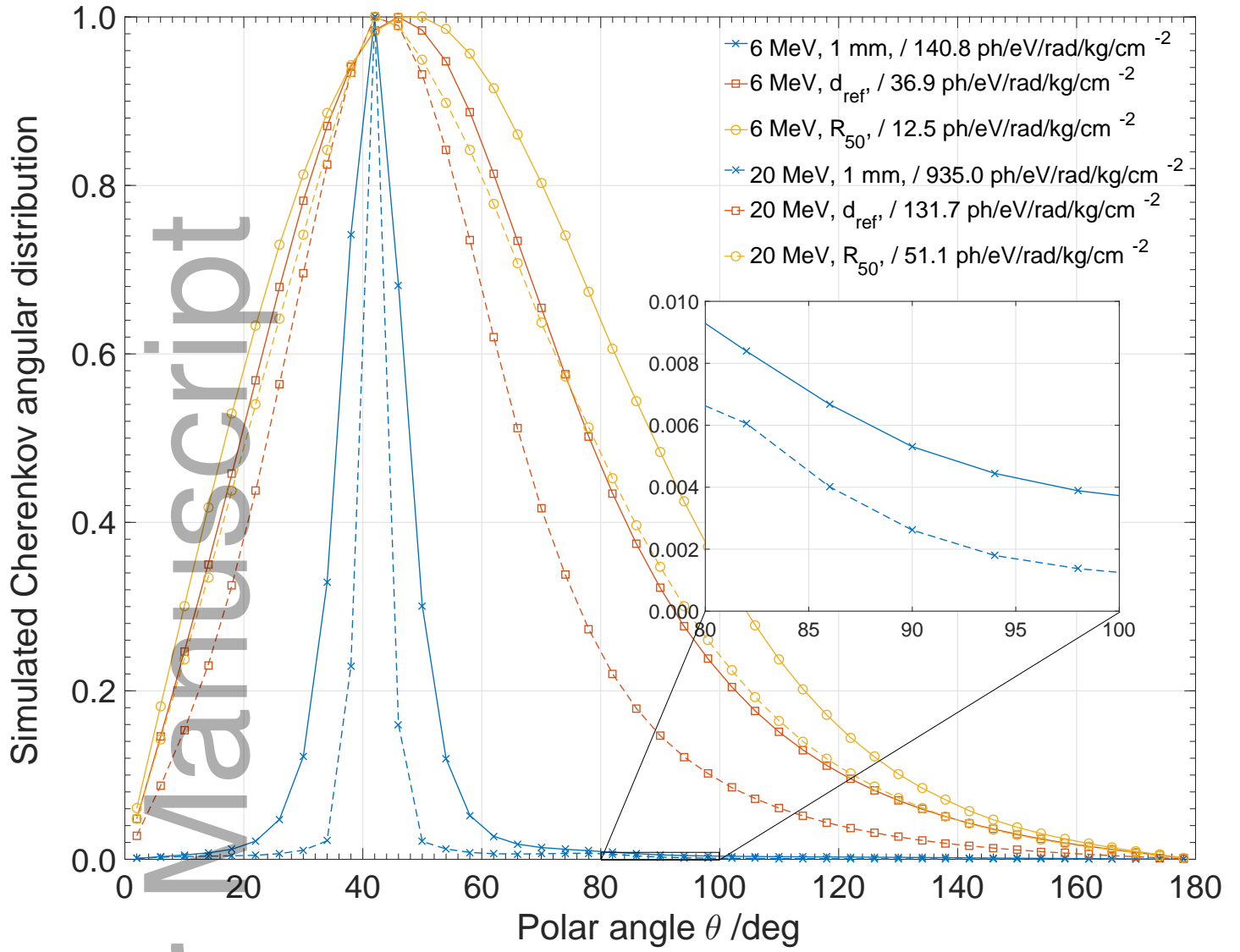


mp_13414_f10.eps

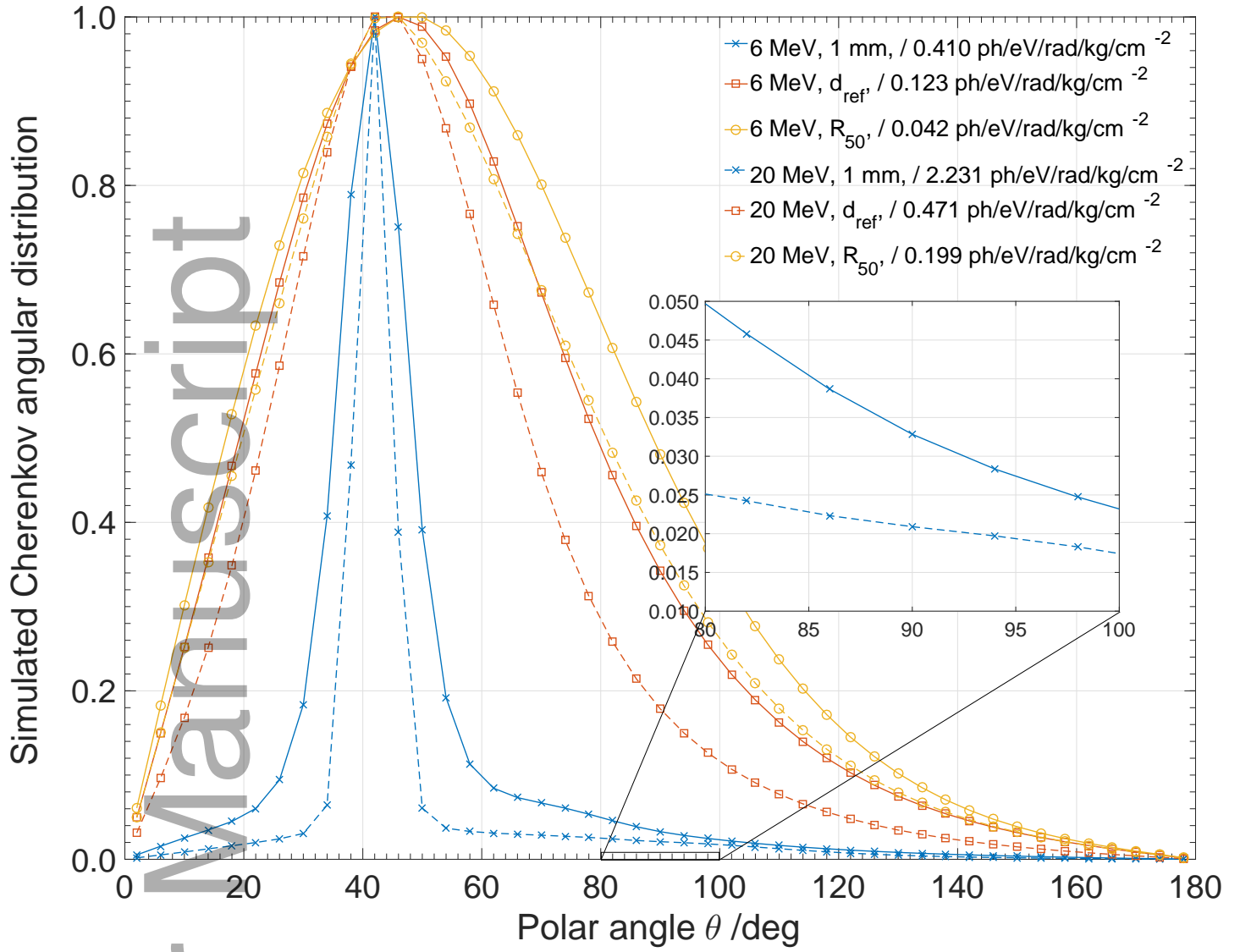


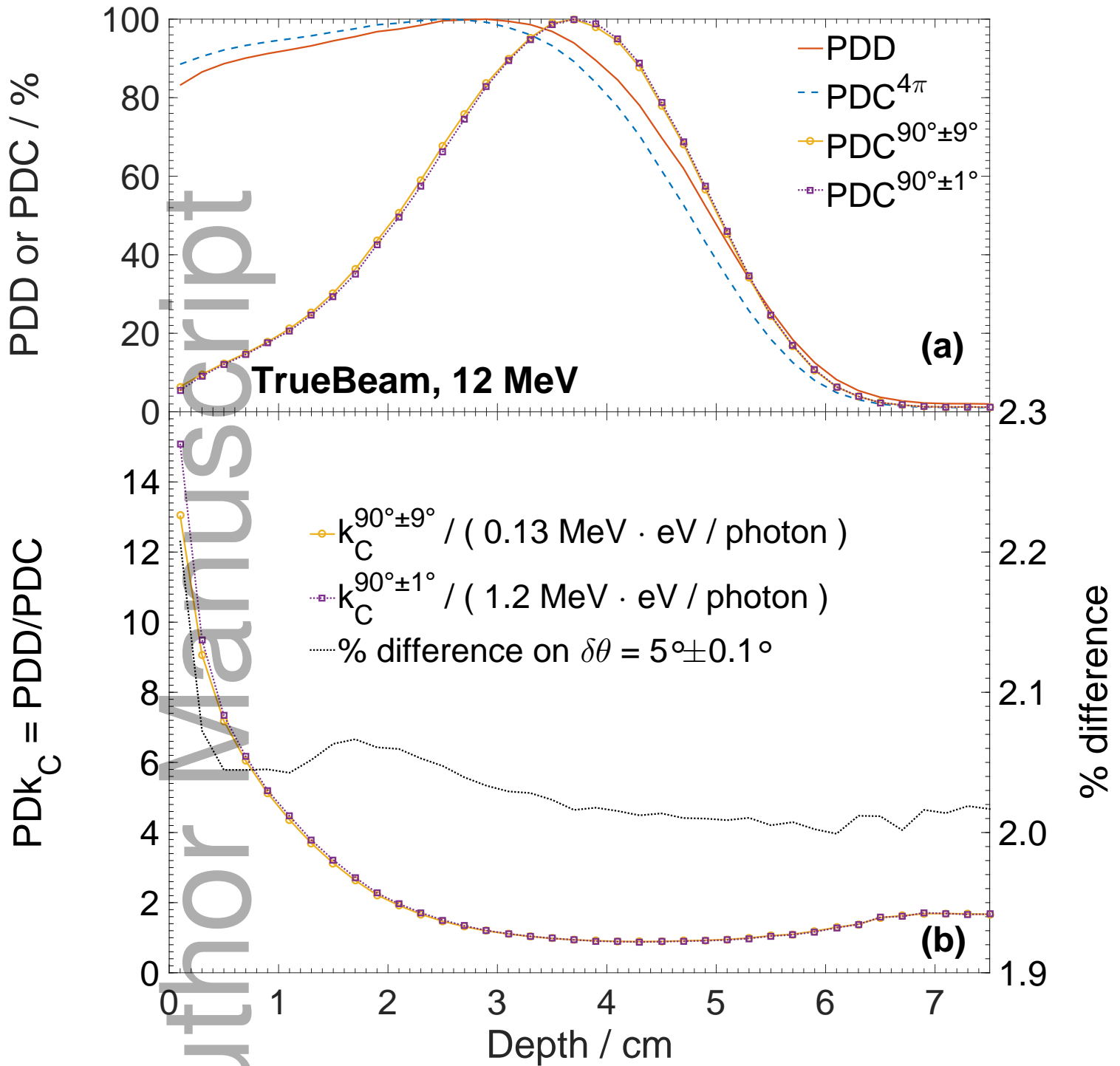
mp_13414_f11.eps



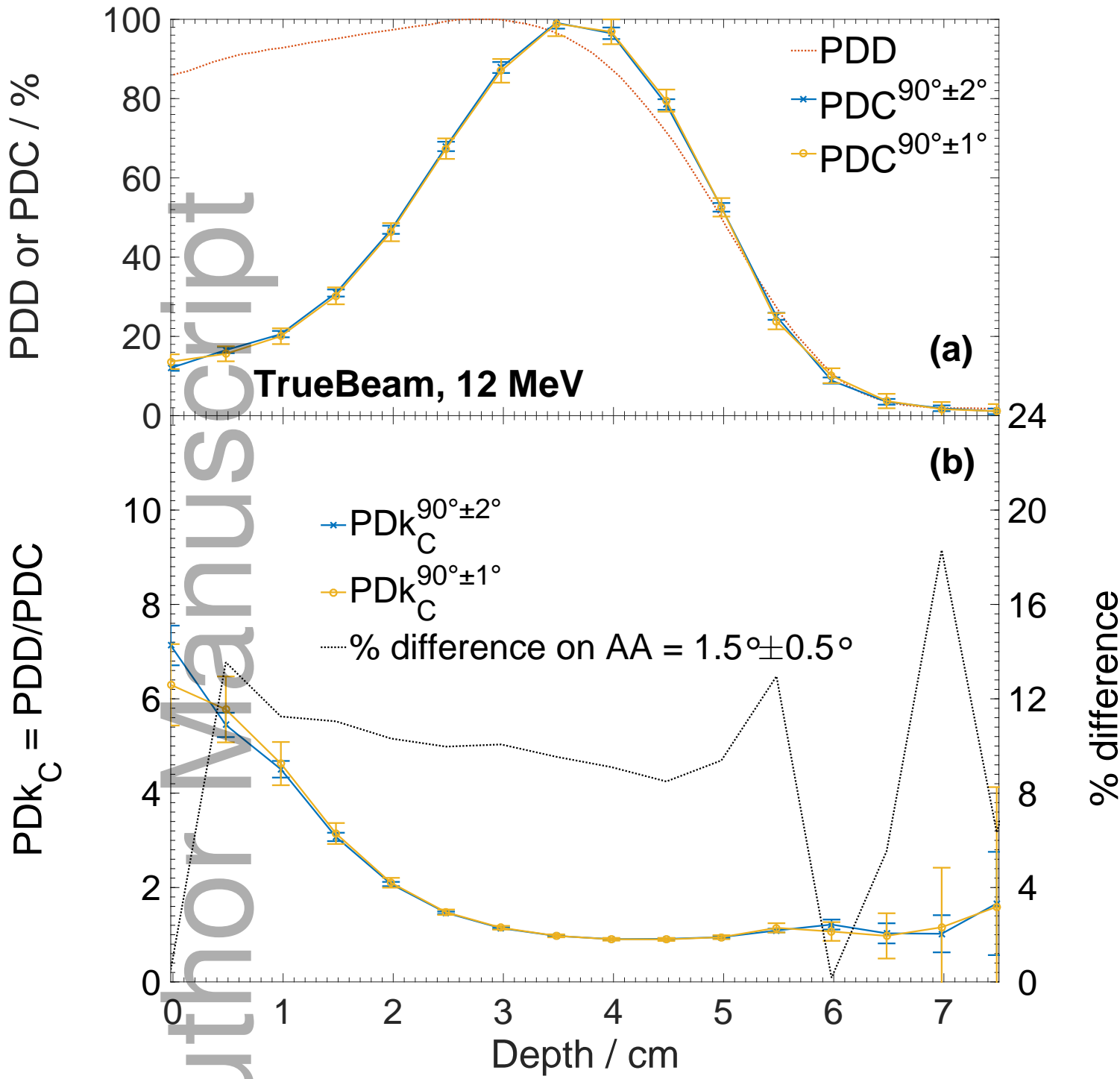


mp_13414_f12b.eps

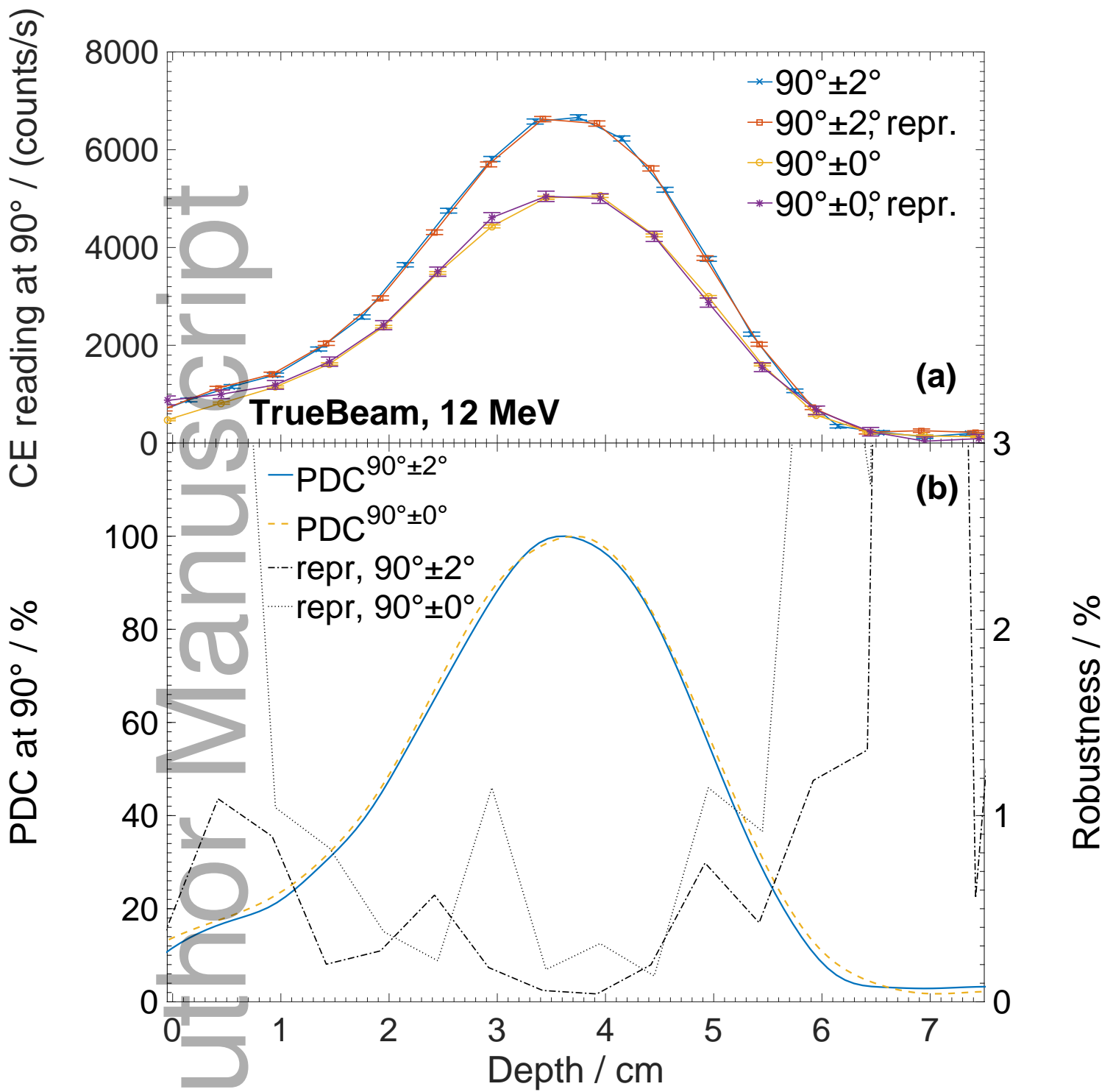




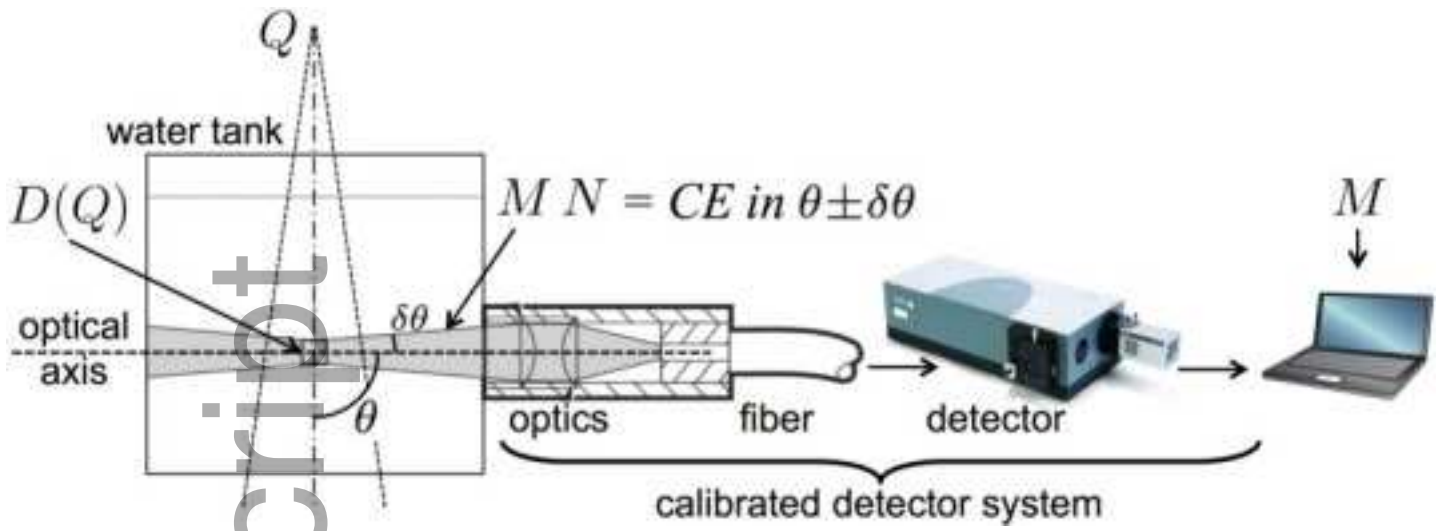
mp_13414_f13.eps



mp_13414_f14.eps

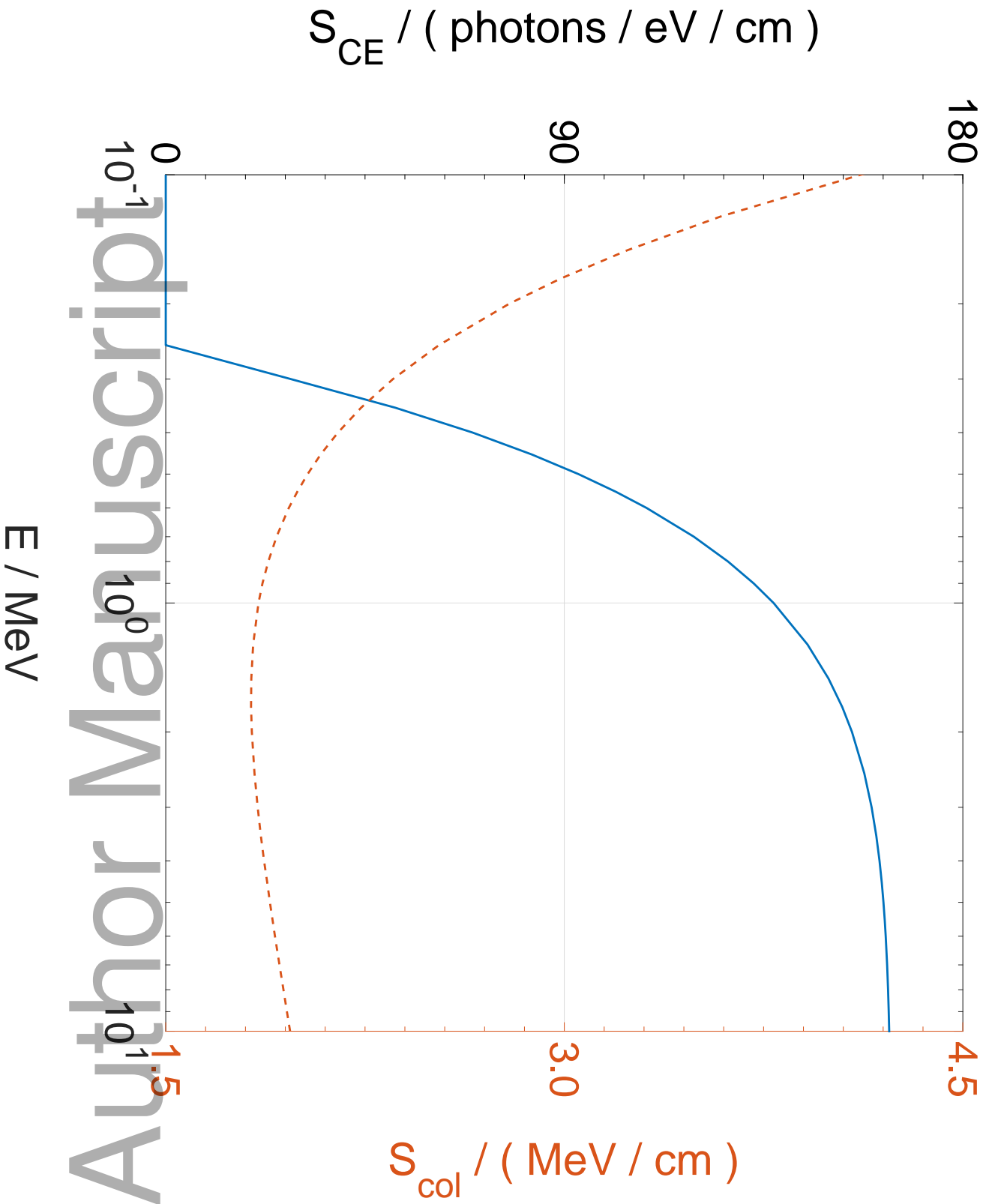


mp_13414_f15.eps

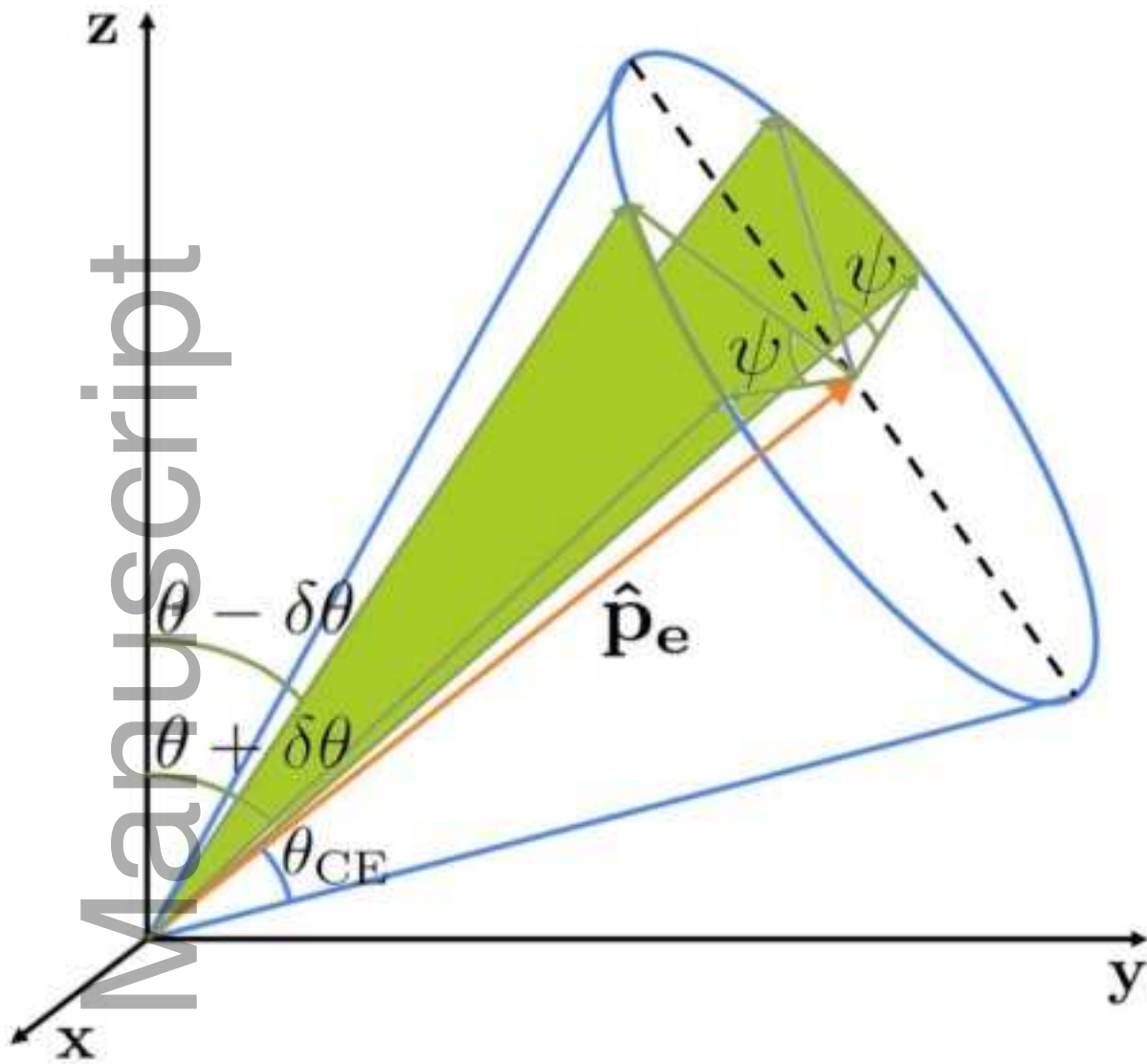


mp_13414_f2.jpg

Author Manuscript



mp_13414_f3.eps

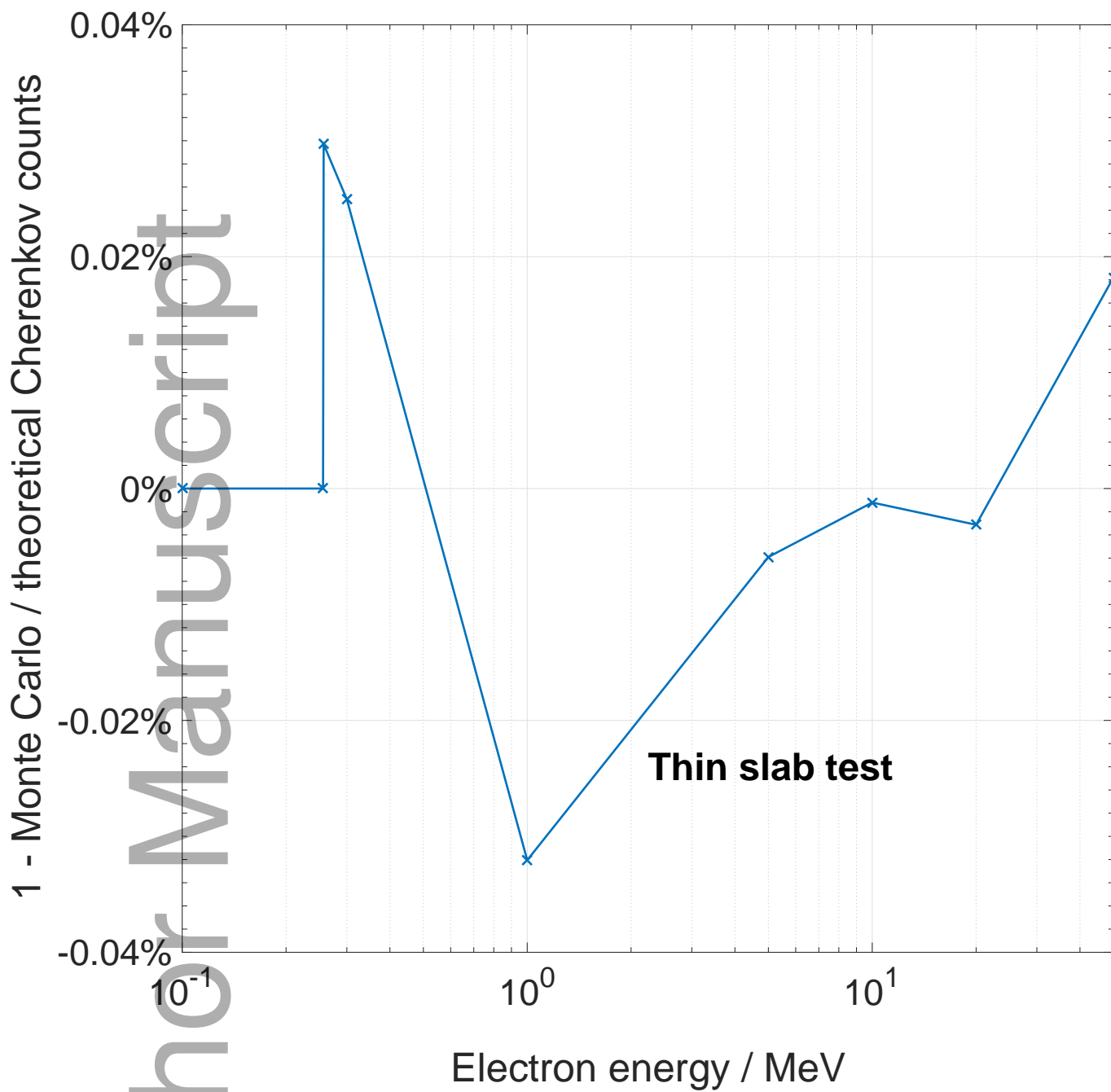


mp_13414_f4.jpg

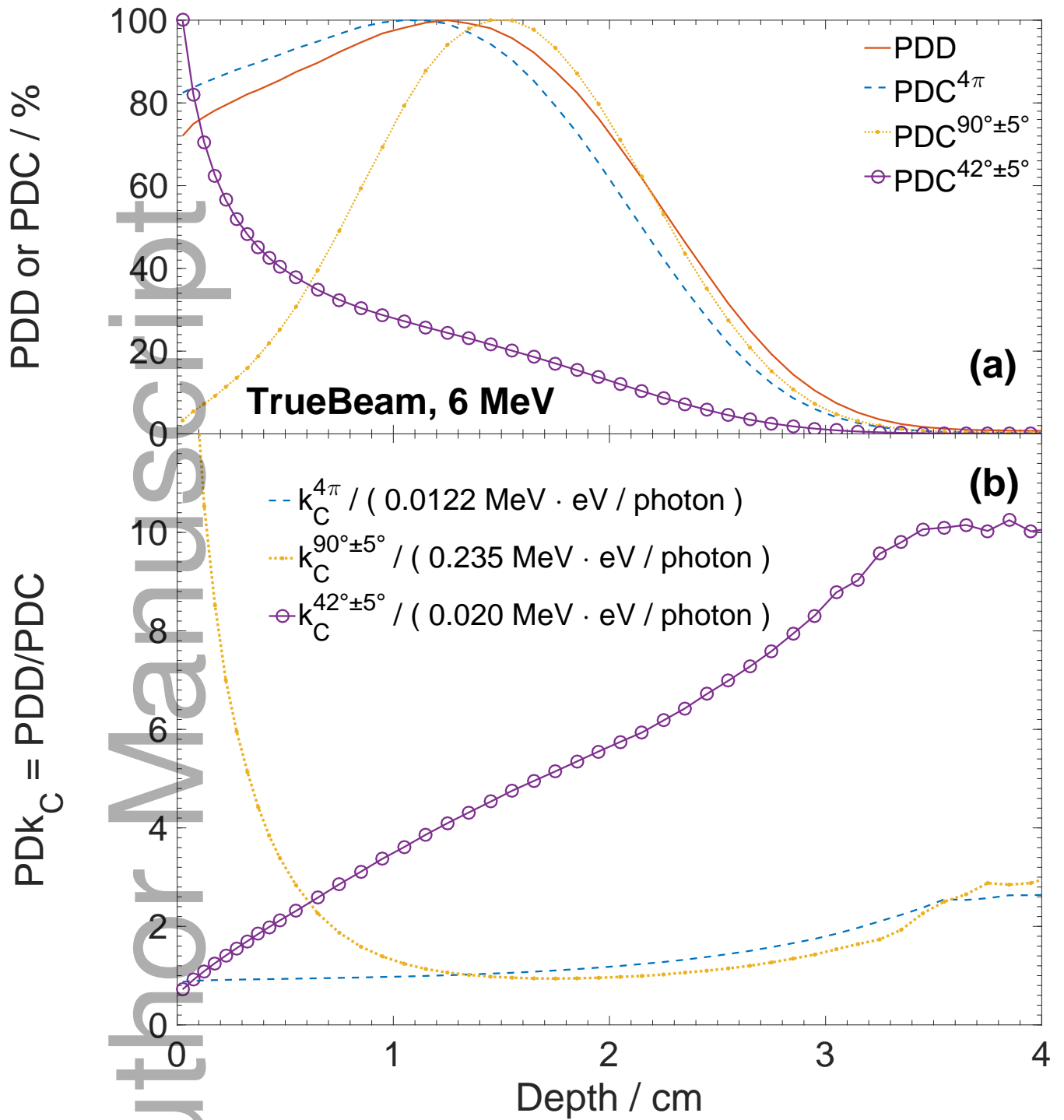


mp_13414_f5.jpg

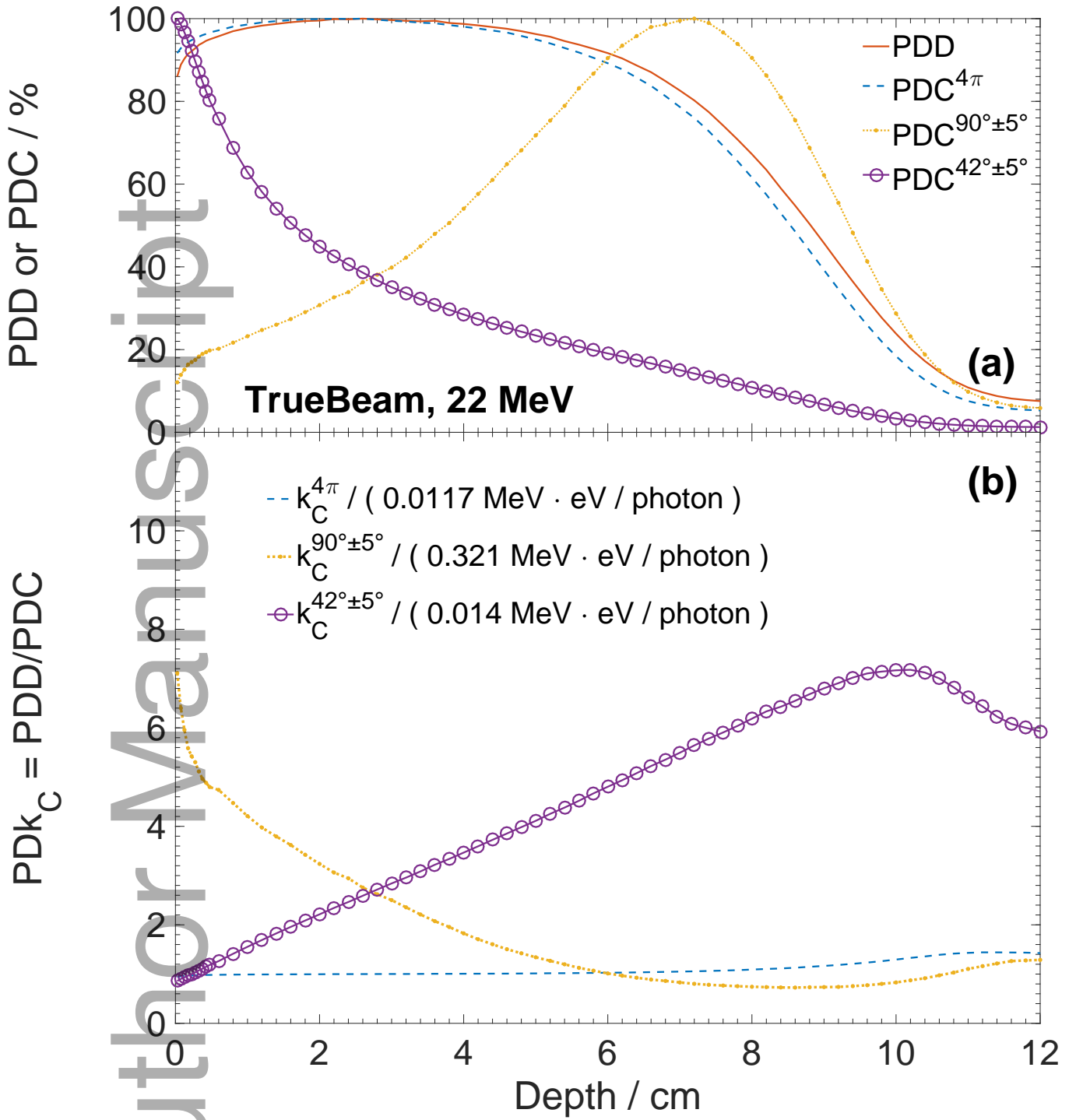
Author Manuscript



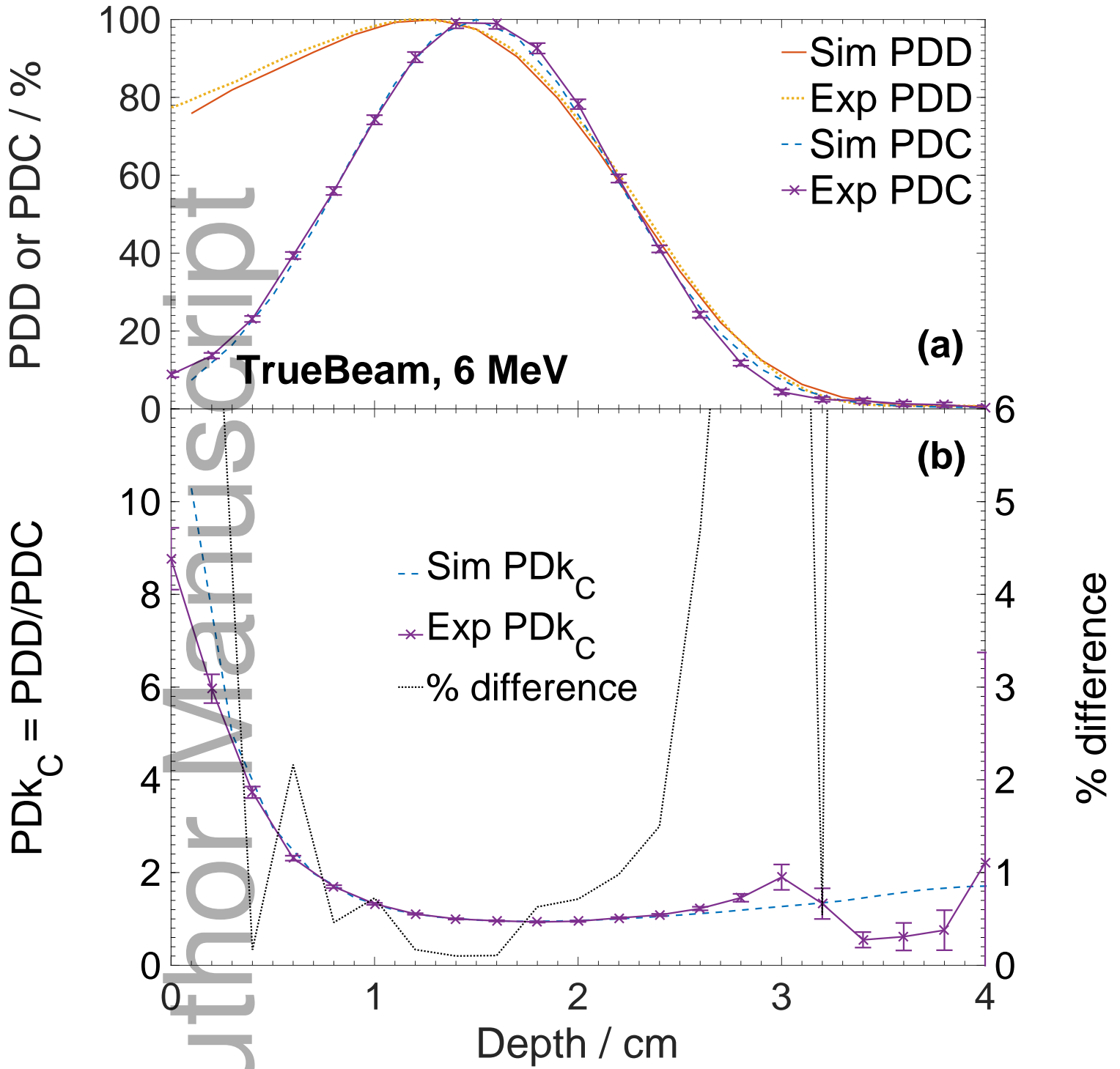
mp_13414_f6.eps



mp_13414_f7.eps



mp_13414_f8.eps



mp_13414_f9.eps